Dynamic assembly of malate dehydrogenase-citrate synthase multienzyme complex in the mitochondria.

Joy Omini,[1] Inga Krassovskaya,[1] Taiwo Dele-Osibanjo,[1] Connor Pedersen,[1] Toshihiro Obata[1*].

1, Department of Biochemistry and Center for Plant Science Innovation, University of Nebraska-Lincoln, 1901 Vine Street, Lincoln, Nebraska 68588, USA

*For correspondence: tobata2@unl.edu (Toshihiro Obata)

Abstract The tricarboxylic acid (TCA) cycle enzymes malate dehydrogenase (MDH1) and citrate synthase (CIT1) form a multienzyme complex, referred to as a metabolon, that channels intermediate oxaloacetate between their reaction centers. Given that the MDH1-CIT1 metabolon enhances pathway reactions in vitro, its dynamic assembly is hypothesized to contribute to TCA cycle regulation in response to cellular metabolic demands. Here, we demonstrated that yeast mitochondrial MDH1 and CIT1 dissociated when aerobic respiration was suppressed by the Crabtree effect and associated when the respiratory activity was enhanced by acetate. Pharmacological TCA cycle inhibition dissociated the complex, whereas electron transport chain inhibition enhanced the interaction. The multienzyme complex assembly was related to the mitochondrial matrix acidification and oxidation, as well as cellular levels of malate, fumarate, and citrate. These factors significantly affected the MDH1-CIT1 complex affinity in vitro. Especially, variations in buffer pH within the physiological pH range between 6.0 and 7.0 in the mitochondrial matrix significantly impacted the MDH1-CIT1 affinity. These results demonstrate the dynamic association and dissociation of the MDH1-CIT1 metabolon and its relationship with respiratory activity, supporting metabolon dynamics as an integral factor in metabolic regulation governed by multiple factors such as mitochondrial pH and metabolite levels.

Introduction

Enzymes catalyzing sequential reactions can interact to form a multienzyme complex, often called a 'metabolon,' which channels the metabolic intermediate within the complex. Metabolite channeling can mediate pathway reactions by concentrating the reaction intermediates near the enzyme active site and sequestering them from competing reactions (Obata, 2020; Spivey and Ovádi, 1999; Wheeldon et al., 2016). Thus, the dynamic assembly of multienzyme complex is believed to quickly regulate cellular metabolic flux by changing their degree of association and dissociation without involving time-consuming and resource-demanding protein synthesis, degradation, and modification (Halper and Srere, 1977; Morgunov and Srere, 1998; Obata, 2019; Omini et al., 2024; Srere, 1985; Sumegi et al., 1993). However, limited experimental evidence shows metabolon dynamics and the mechanisms regulating its association.

The tricarboxylic acid (TCA) cycle multienzyme complex composed of malate dehydrogenase (MDH) and citrate synthase (CS) is conserved in all organisms analyzed so far, including animals, bacteria, yeast, and plants (Meyer et al., 2011; Morgunov and Srere, 1998; Robinson et al., 1987; Zhang et al., 2017). MDH and CS catalyze the key steps in respiratory metabolism as their reactions comprise the carbon entry steps from the glycolytic processes as malate and acetyl-CoA, respectively (Sweetlove et al., 2010). MDH-CS complex is considered a dynamic protein complex (Bulutoglu et al., 2016; Omini et al., 2021) that protects the channeled intermediate, oxaloacetate, from degradation and competing pathways in the bulk phase of the cell (Bulutoglu et al., 2016). Importantly, MDH-CS complex formation and oxaloacetate channeling are considered essential for the forward TCA cycle flux to occur since MDH forward reaction to synthesize oxaloacetate is thermodynamically unfavorable in physiological conditions (Fukuda et al., 2008). These findings suggest that the dynamic association and dissociation of the MDH-CS multienzyme complex play a role in coordinating the TCA cycle and associated metabolic pathways. To address this hypothesis, this study focuses on demonstrating the in vivo dynamics of the MDH-CS complex in relation to respiratory states, a crucial aspect of achieving metabolic regulation. Another key

requirement, the direct impacts of the metabolon on pathway flux, will be addressed in a separate study.

This study utilized the yeast mitochondrial MDH (MDH1)-CS (CIT1) multienzyme complex as the model. Budding yeast, *Saccharomyces cerevisiae*, dramatically rearranges its central carbon metabolism in response to changes in nutrient availability and stress conditions (Causton et al., 2001; Rep et al., 1999; Rolland et al., 2002). Remarkably, yeast respiratory metabolism, involving aerobic respiration and fermentation, is highly adaptable to substrate availability (Pfeiffer and Morley, 2014). When oxygen and non-fermentable respiratory substrates, such as acetate, are abundant, aerobic respiration is upregulated, with increased carbon flux through the TCA cycle (Gerstmeir et al., 2003; Lee et al., 2011). In the presence of fermentable sugars, such as glucose and fructose, the fermentation pathway is upregulated, and aerobic respiration is repressed, even when oxygen is available (Zhang et al., 2022). Furthermore, aerobic respiration and fermentation cooperate in the presence of a poorly fermentable carbon source like raffinose (Guaragnella et al., 2013). Application of fermentable substrates to respiring yeast cells induces a substantial shift from aerobic respiration to fermentation, known as the 'Crabtree effect,' involving a massive transcriptional rearrangement of enzyme genes related to aerobic respiration and fermentation (Gancedo, 1998; Ronne, 1995; Thierie and Penninckx, 2010). This inducible metabolic shift in yeast makes it an ideal model for investigating the dynamic relationship between the MDH1-CIT1 multienzyme complex and TCA cycle flux. Understanding the mechanisms of the Crabtree effect is crucial for metabolic engineering applications to enhance the supply of TCA cycle intermediates for desired product synthesis (Yin et al., 2015) and for gaining insights into metabolic regulation in other eukaryotic systems, including cancer cells, which exhibit metabolic shifts similar to the Crabtree effect (Diaz-Ruiz et al., 2011).

Various allosteric regulators and environmental factors, including pH and redox state, affect MDH and CS enzyme activities (Beeckmans, 1984; Williamson and Cooper, 1980). These factors alter protein conformations, influencing the MDH-CS complex affinities. Previous in vitro studies have demonstrated that NAD^+, malate, succinate, acetyl-CoA, α-ketoglutarate, and acidic pH enhance the MDH-CS interaction, while NADH, citrate, and basic pH weaken it (Omini et al., 2024, 2021; Tompa et al., 1987; Wu and Minteer, 2015). These allosteric regulators promote the MDH-CS interaction when the TCA cycle substrates are abundant and products are limited, indicating the role of the MDH-CS multienzyme complex in the TCA cycle feedback regulation. The electron transport chain activity affects the mitochondrial matrix pH, redox state, and ATP content and is closely related to cellular respiratory flux distributions (Santo-Domingo and Demaurex, 2012)). Therefore, the MDH-CS multienzyme complex may associate and dissociate according to the microenvironment in the mitochondrial matrix, such as metabolite concentrations, pH, redox state, and energy levels.

We adopted a NanoBiT protein-protein interaction assay system (Dixon et al., 2016) to monitor real-time multienzyme complex interactions in living yeast cells using continuous microplate readings. The NanoBiT split-luciferase system is based on the 18 kDa NanoLUC luciferase derived from deep-sea shrimp. The small size of this reporter is designed to minimize structural and behavioral interference with the target proteins, while offering a dynamic range and brightness approximately 150-fold greater than those of conventional luciferases, enabling detection of weak, transient interactions. The NanoBiT subunits exhibit low intrinsic affinity (K_D = 190 μM) and rapid association and dissociation kinetics (k_{on} = 500 $M^{-1}s^{-1}$, k_{off} = 0.2 s^{-1}), ensuring that the luminescent complex formation is dictated by the interaction of the fused proteins rather than the affinity of the tags themselves (Dixon et al., 2016). While other fluorescence-based methods, such as FLIM-FRET and BRET, are widely used for *in vivo* protein-protein interaction studies, they are limited in yeast microplate assays due to high cellular autofluorescence. The

NanoBiT system overcomes these constraints, providing semi-quantitative monitoring of relative fluctuations in protein interaction levels over time across a diverse range of metabolic conditions.

In this study, the NanoBiT system examined the MDH1-CIT1 multienzyme complex association in the presence of various carbon sources and respiratory inhibitors. The results showed the relationship between respiratory activity and the dynamic MDH1-CIT1 complex assembly. Analysis of the mitochondrial matrix microenvironment using fluorescent biosensors and cellular metabolite profiles revealed crosstalk among cellular respiratory status, the MDH1-CIT1 interaction, and the mitochondrial matrix microenvironment, including pH. These findings indicate the functional dynamics of the MDH-CS multienzyme complex and how they coordinate with the metabolic states of the TCA cycle and adjacent pathways.

Results

MDH1-CIT1 interaction was detected exclusively in respiratory conditions.

We employed a NanoBiT split-luciferase system (Dixon et al., 2016) for semi-quantitative relative detection of the MDH1-CIT1 multienzyme complex association in living yeast cells. The codon-optimized sequences of nano-BIT subunits were integrated into the direct downstream of the MDH1 and CIT1 exons in the yeast genome by gene homologous recombination to fuse the NanoBiT subunits to the native enzymes. The NanoBiT subunits reconstitute the NanoLUC holoenzyme to produce luciferase signals when MDH1 and CIT1 are in proximity. The affinity between the NanoBiT subunits is very low and does not stabilize the interactions of the tagged proteins (Dixon et al., 2016). The integration of NanoBiT subunits had no significant effect on the cellular growth rate or cellular MDH and CS enzyme activities (Figure 1 – figure supplement 1). Although the MDH1-CIT1 reporter line did not show a detectable luciferase signal when it was grown in a fermentation condition (glucose-containing SD media; SD-Gluc), it showed a substantial luciferase signal in mixed-respiration (raffinose-containing SD media; SD-Raff) and respiration (acetate-containing SD media; SD-Acet) conditions (Figure 1A). These results indicate that MDH1 and CIT1 interact under respiratory conditions. The MDH1-CIT1 interaction can be related to the oxidative respiration and the TCA cycle activity since oxygen consumption was detected only in SD-Raff and SD-Acet media but not in the SD-Gluc medium (Figure 1B), as previously reported (Klein et al., 1998; Polakis and Bartley, 1965; Rep et al., 1999; Rolland et al., 2002; Strittmatter, 1957). However, MDH1 and CIT1 expressions were downregulated in SD-Gluc growing cells near the detection limit (Figure 1C), making it difficult to conclude if the undetectable MDH1-CIT1 interaction was due to complex dissociation or low protein levels.

Crabtree induction reduced the MDH1-CIT1 interaction.

To test the relationship between respiratory activity and the MDH1-CIT1 complex association when MDH1 and CIT1 enzymes are abundant in the cell, we monitored the time course of the MDH1-CIT1 interaction after a rapid shift from aerobic to anaerobic respiration via the Crabtree effect. The Crabtree effect was induced by applying 2% glucose to the SD-Raff-grown MDH1-CIT1 NanoBiT reporter line (Figure 2, Figure 2 – figure supplement 1). The luciferase signals only slightly changed for 30 min upon glucose application, followed by a steep decline. In contrast, the control cells retained the initial signal level for 100 min (Figure 2A, Figure 2 – figure supplement 1D). Decrease in the MDH1-CIT1 interaction was validated by a co-immunoprecipitation assay at 1.5 and 2.5 hours after the glucose application (Figure 2 – figure supplement 1A). Other Crabtree inducers, such as fructose and sucrose, also reduced the MDH1-CIT1 interaction, while the addition of non-fermentable sugars, including galactose, caused no significant change in MDH1-CIT1 interaction (Figure 2 – figure supplement 2A-D, Figure 2 – figure supplement 3), likely due to raffinose in the media suppressing its effects. The signal decline following glucose application was partially reversed by co-application with a fermentation inhibitor, 100 mM phosphate (van Urk et al., 1989; Figure 2A). Phosphate co-application slowed the decrease of luciferase signal compared to the glucose-applied cells, and the signal was not statistically significantly lower than the control until 80 min after application. The oxygen consumption rate significantly decreased when glucose was added to SD-Raff-grown cells but was slightly recovered by co-application of

156 glucose with phosphate (Figure 2 – figure supplement 2E). These results indicate that the
157 respiratory suppression by the Crabtree effect is related to MDH1-CIT1 complex disruption.
158
159 MDH1 protein level monitored with the yeast strain expressing MDH1 fused with full-length
160 NanoLUC luciferase showed a 20% decline within 100 min upon glucose addition (Figure 2,
161 Figure 2 – figure supplement 1B). Western blotting also showed a slight decrease in the MDH1
162 and CIT1 levels (Figure 2 – figure supplement 1C). The time course of the MDH1-CIT1 NanoBiT
163 signal was inconsistent with that of MDH1-NanoLUC, and the 20% decline in protein content
164 cannot fully explain the decrease of MDH1-CIT1 signal by over 50% within 100 min after glucose
165 addition (Figure 2A, Figure 2 – figure supplement 1B). The reduction of MDH1-CIT1 interaction
166 was not accompanied by the MDH1 and CIT1 abundance in a repeated experiment (Figure 2 –
167 figure supplement 1D-E). The interaction index, calculated by normalizing the NanoBiT signal to
168 MDH1 and CIT1 abundances measured with MDH1-NanoLUC and CIT1-NanoLUC (see
169 Materials and Methods), showed reduced interaction after 60 min of glucose application.
170 Therefore, the decline in the MDH1-CIT1 NanoBiT signal reflects the MDH1-CIT1 complex
171 dissociation co-occurring with the Crabtree effect, even though we cannot exclude a partial effect
172 of protein degradation (Litsios et al., 2018).
173
174 Oxidative respiration significantly influences the microenvironments in the mitochondrial matrix
175 (Beeckmans, 1984; Williamson and Cooper, 1980). To assess if the MDH1-CIT1 interaction
176 decline is related to the changes in the microenvironments of the mitochondrial matrix by the
177 Crabtree effect, we monitored the mitochondrial matrix pH, ATP concentration, and redox state by
178 expressing fluorescent biomarkers, pHluorin, mito-GoAteam2, and mito-roGFP1, respectively, in
179 the mitochondrial matrix of the MDH1-CIT1 reporter line (Figure 2 – figure supplement 4A-D).
180 Mitochondrial matrix pH in the SD-Raff-grown cells was 7.2 and temporally declined to 6.8 in the
181 first 25 min of glucose application. The control cell matrix pH gradually decreased to 6.2 and
182 remained lower than in glucose-applied cells (Figure 2B). The alterations of the MDH1-CIT1
183 interaction and mitochondrial matrix parameters in the control condition are not due to carbon
184 starvation, since 2% raffinose application had no significant effect (Figure 2 – figure supplement
185 4E). The redox state stayed around -288.0 mV in both the control and glucose cells (Figure 2C).
186 The ATP level slightly increased during the experimental period of 100 min in both the control and
187 glucose cells, with slightly but significantly lower levels in the glucose than in the control cells
188 from 55 min to 100 min (Figure 2D). Thus, mitochondrial matrix pH and ATP levels were
189 maintained after glucose was applied to cells, while they decreased and increased in control cells
190 during the experimental period, indicating that mitochondrial pH and ATP levels are associated
191 with MDH-CS complex dissociation during the Crabtree induction.
192
193 Our previous in vitro study showed that metabolite abundance influences the MDH-CS complex
194 interaction (Omini et al., 2021). To assess the possible roles of metabolite accumulation in
195 controlling MDH1-CIT1 complex interaction, we determined the cellular levels of 38 metabolites
196 (Data S1) by gas chromatography-mass spectrometry (GC-MS). We focus here on the
197 intermediates of the TCA cycle and related pathways (Figure 2E). At 80 min after 2% glucose
198 application to SD-Raff-grown cells, malate, citrate, fumarate, and glutamate levels decreased,
199 while α-ketoglutarate content increased significantly compared to the control cells (Figure 2G).
200 Thus, the glucose-induced shift from aerobic respiration to fermentation altered the intracellular
201 metabolite profile in SD-Raff-grown cells, potentially influencing the MDH1-CIT1 affinity.
202
203 **MDH1-CIT1 complex interacts in relation to the TCA cycle activity.**
204 We further assessed the relationship between the MDH1-CIT1 complex association and TCA
205 cycle activity. Acetate supplies acetyl-CoA to the TCA cycle and enhances its activity (Cavero et
206 al., 2003). The application of 1% sodium acetate gradually increased the MDH1-CIT1 interaction
207 while MDH1 and CIT1 protein abundance slightly reduced (Figure 3A, Figure 3 – figure
208 supplement 1 A-D). The TCA cycle activation by ethanol (Schüller, 2003) also enhanced the
209 complex association (Figure 3 – figure supplement 1E). However, it is accompanied by an
210 increase in MDH1 and CIT1 abundance (Figure 3 – figure supplement 1F&G), making the effects

211 of ethanol on the complex association unclear (Figure 3 – figure supplement 1H). On the other
212 hand, TCA cycle inhibition by 5 mM sodium arsenite, which impedes α-ketoglutarate
213 dehydrogenase (Lee et al., 2011), led to a decline in MDH1-CIT1 interaction within 10 min (Figure
214 3B, Figure 3 – figure supplement 1 I-L). Aminooxyacetate (AOA) is an aminotransferase inhibitor
215 and reduces TCA cycle activity by blocking the malate-aspartate NADH shuttle, which intersects
216 with the cycle (Borst, 2020; Eto et al., 1999; Molinié et al., 2022). The MDH1-CIT1 interaction
217 gradually reduced following 0.5 mM AOA application (Figure 3C, Figure 3 – figure supplement
218 1M-P). These results support that the MDH1-CIT1 multienzyme complex association is related to
219 TCA cycle activity.
220
221 Mitochondrial matrix pH declined to 6.1 immediately after acetate application (Figure 3D).
222 Mitochondrial pH went slightly lower than that of the control cells after 40 min of TCA cycle
223 inhibition by arsenite (Figure 3E), while AOA application had no effect on mitochondrial pH
224 (Figure 3F). The mitochondrial matrix redox state was gradually increased in the control cells
225 during the experimental period, while it was kept constant in the cells treated by acetate, arsenite,
226 and AOA (Figure 3G-I), resulting in the significantly lower mitochondrial matrix redox state in the
227 treated cells in the latter half of the experimental period. Mitochondrial ATP level was decreased
228 by acetate treatment after 40 min (Figure 3J), although arsenite and AOA showed no effect on
229 the mitochondrial ATP levels within the experimental period (Figure 3J&K). These changes in
230 mitochondrial microenvironments did not show clear, direct relationships with the MDH1-CIT1
231 interaction.
232
233 We evaluated the cellular metabolite profile after treatment of SD-Raff grown cells for 80 min with
234 1% acetate, 5mM arsenite, and 0.5 mM AOA to determine the relationship between change in
235 metabolite levels and the MDH1-CIT1 complex interaction (Figure 3M). Acetate application
236 significantly reduced malate, α-ketoglutarate, fumarate, succinate, and glutamate levels, while
237 aspartate abundance significantly increased. Inhibition of the TCA cycle by arsenite significantly
238 reduced the levels of all TCA cycle metabolites other than α-ketoglutarate. Aspartate and
239 glutamate were also decreased, and glutamate was almost depleted in the cell (Figure 3M). AOA
240 significantly decreased citrate, fumarate, and succinate levels while it increased α-ketoglutarate
241 abundance (Figure 3M). Reduction of TCA cycle organic acids by the TCA cycle inhibition may be
242 related to the reduction in the MDH1-CIT1 interaction.
243
244 **Electron transport chain inhibition enhanced the MDH1-CIT1 interaction, coinciding with**
245 **matrix acidification.**
246 Mitochondrial electron transport chain (ETC) activity is directly related to the mitochondrial
247 microenvironments (Selivanov et al., 2008). To further assess the effects of mitochondrial matrix
248 microenvironments on MDH1-CIT1 complex interaction, we treated SD-Raff-grown cells with ETC
249 inhibitors. Inhibition of ETC complex II, III, IV, and V with 20 mM malonate, 10 μM antimycin, 0.5
250 mM cyanide, and 1 mM oligomycin, respectively, significantly reduced oxygen consumption of
251 SD-Raff-grown cells (Figure 4 – figure supplement 1), showing their effects on respiration. MDH1-
252 CIT1 interaction was enhanced by ETC inhibitors with minor alterations of MDH1 and CIT1
253 protein levels (Figure 4A-C, Figure 4 – figure supplement 2), whereas the complex V (ATP
254 synthase) inhibitor exerted no effect on MDH1-CIT1 interaction and mitochondrial matrix
255 microenvironment in this experimental condition (Figure 4 – figure supplement 3A-D). Complex II
256 inhibition slightly and temporally enhanced the MDH1-CIT1 interaction, although the increase was
257 not statistically significant compared to the control (Figure 4A, Figure 4 – figure supplement 1B-
258 E). The MDH1-CIT1 interaction was enhanced in the first 20 min of complex IV inhibition and
259 reduced to the basal level afterward (Figure 4B, Figure 4 – figure supplement 2E-H). Complex III
260 inhibition by antimycin slowly increased MDH1-CIT1 interaction, and the signal increase peaked
261 at 60 min of treatment (Figure 4C; Figure 4 – figure supplement 2I-L).
262
263 Mitochondrial matrix pH was reduced by all ETC inhibitor treatments (Figure 4D-F), although the
264 effect was very small in malonate-treated cells (Figure 4D). The matrix pH was transiently
265 decreased and exhibited an inverse relationship with the MDH1-CIT1 interaction (Figure 4E). The

266 mitochondrial matrix pH was reduced to 5.5 immediately after antimycin application and remained
267 at the same level for 100 min (Figure 4F). These treatments show minor effects on the redox
268 state of the mitochondrial matrix (Figure 4 G-I). The matrix was gradually oxidized following
269 antimycin treatment, but the difference relative to control cells was not statistically significant
270 (Figure 4I). ETC inhibitions also showed relatively minor effects on mitochondrial ATP levels
271 (Figure 4J-L), except for the reduction of ATP levels at the first 20 min of Complex IV inhibition
272 (Figure 4K), which is accompanied by the increase of MDH1-CIT1 interaction (Figure 4B). These
273 results indicate the relationship between MDH1-CIT1 interaction and mitochondrial matrix
274 acidification.
275
276 Since the results indicate a relationship between mitochondrial matrix pH and the MDH1-CIT1
277 interaction, we have tested the effect of an uncoupler, carbonyl cyanide 3-chlorophenylhydrazone
278 (CCCP), on this interaction (Figure 4 – figure supplement 4), which is expected to equilibrate the
279 mitochondrial pH with the medium pH of 5.8 (Rosado et al., 2008). Treatment with 2 μM CCCP
280 increased the MDH1-CIT1 interaction signal, suggesting that acidic pH enhances complex
281 association (Figure 4 – figure supplement 4A&D). However, this result should be interpreted with
282 caution, as CCCP treatment compromised the luciferase signal from MDH1 and CIT1 fused to
283 full-length NanoLUC (Figure 4 – figure supplement 4B&C).
284
285 Cellular metabolite profiles were determined 30 min after malonate and cyanide treatments and
286 80 min after antimycin and oligomycin treatments. Complex II and V inhibition did not significantly
287 alter cellular metabolite levels other than the malate and aspartate accumulation in malonate-
288 treated cells (Figure 4M, Figure 4 – figure supplement 3E). Complex IV inhibition by cyanide
289 significantly reduced citrate and glutamate levels, while malate, alpha-ketoglutarate, fumarate,
290 and succinate levels significantly increased (Figure 4M). Complex III inhibition significantly
291 decreased citrate and α-ketoglutarate levels and increased the malate level (Figure 4M). These
292 results support the relationship between the levels of TCA cycle intermediates and MDH1-CIT1
293 interaction.
294
295 **MDH1-CIT1 interaction is affected by pH, ATP concentration, and metabolite availability in**
296 **vitro.**
297 To evaluate the specific effects of microenvironments and metabolite availability on the MDH1-
298 CIT1 interaction, we investigated the MDH1-CIT1 affinity in vitro using recombinant proteins.
299 Acidic pH significantly enhanced the binding affinity of the MDH1-CIT1 complex (Figure 5A) within
300 the physiological range observed in this study (Figure 2B, Figure 3D, Figure 4D, E, F). The K_d of
301 the MDH1-CIT1 interaction was 3.48 μM at pH 7.2, while it was one magnitude lower at acidic pH
302 (0.223 μM at pH 6.4 and 0.033 μM at pH 6.0). We also assessed the effects of the metabolites on
303 the MDH1-CIT1 interaction (Figure 5B, Figure 5 – figure supplement 1). We tested malate,
304 fumarate, citrate, α-ketoglutarate, succinate, glutamate, and aspartate since their cellular levels
305 changed when the MDH1-CIT1 interaction altered (Figure 2E, Figure 3M, Figure 4M). Citrate
306 destroyed the MDH1-CIT1 interaction, while malate and fumarate significantly enhanced complex
307 affinity (Figure 5B). α-ketoglutarate, succinate, and aspartate slightly enhanced MDH1-CIT1
308 complex affinity, although glutamate did not affect the interaction (Figure 5 – figure supplement
309 1A). ATP also enhanced the MDH1-CIT1 complex affinity (Figure 5 – figure supplement 1B) as
310 observed in porcine enzymes (Omini et al., 2021). Thus, malate, fumarate, citrate, ATP levels,
311 and pH potentially influence the MDH1-CIT1 interaction in yeast mitochondria.
312
313 **Discussion**
314 Here, we report the relationships between respiratory activity and mitochondrial MDH1-CIT1
315 multienzyme complex interaction in living yeast cells. MDH1-CIT1 multienzyme complex
316 dynamically associated and dissociated in response to respiratory status. This study is the first in
317 vivo evidence in any organism showing the dynamic association and dissociation of the TCA
318 cycle metabolon in real time. The MDH-CS metabolon, specifically, is considered essential for the
319 forward TCA cycle flux due to its ability to overcome the unfavorable thermodynamics of MDH
320 reaction under physiological oxaloacetate concentrations (Beeckmans and Kanarek, 1981; Huang

et al., 2018). The results of this study demonstrate that the MDH1-CIT1 multienzyme complex associates when the TCA cycle is active and dissociates when it is suppressed, supporting the idea that metabolon dynamics are related to pathway regulation. Given that the MDH-CS metabolon is proposed to enhance pathway reactions (Bulutoglu et al., 2016; Fukuda et al., 2008), its dynamic assembly and disassembly would influence pathway activity. Together, these observations align with the proposed theory that metabolon dynamics act as a regulatory mechanism of metabolic flux (Noor et al., 2014; Obata, 2020).

The MDH1-CIT1 complex dissociated under conditions suppressing the TCA cycle. TCA cycle inhibition by arsenite and AOA induced dissociation of the MDH1-CIT1 complex (Figure 3B&C). In a physiological condition, the MDH1-CIT1 complex dissociated when Crabtree-inducing fermentable sugars were supplied to the media (Figures 1, 2, and Figure 2 – figure supplement 1-3). The Crabtree effect redistributes respiratory flux to stimulate fermentation and repress aerobic respiratory pathways, including the TCA cycle (Gancedo, 1998; Ronne, 1995). The metabolic shift by the Crabtree effect is a concerted action of multiple mechanisms, such as the suppression of enzyme gene expressions and the inhibition of mitochondrial transporters (Ahmadzadeh et al., 1996). Interestingly, glucose-induced rapid repression of mitochondrial respiration occurs at a rate that is too great to be explained only by the inhibition of enzyme synthesis, and additional forms of regulation are anticipated to be involved (Ahmadzadeh et al., 1996). The dissociation of the TCA cycle metabolon coincided with this repression (Figure 2A), highlighting metabolon dynamics as a potential additional mechanism to swiftly downregulate mitochondrial respiration during the Crabtree effect.

On the other hand, the MDH1-CIT1 complex interaction was enhanced under conditions that activate the TCA cycle. An increase in TCA cycle activity by the addition of acetate (Orlandi et al., 2014; Vilela-Moura et al., 2011) enhanced the MDH1-CIT1 complex interaction (Figure 3A), suggesting the role of the MDH-CS metabolon in facilitating TCA cycle activity.

However, ETC inhibitions also increased MDH1-CIT1 interaction (Figure 4A-C), despite their inhibitory effects on oxidative respiration (Figure 4 - figure supplement 1) and the TCA cycle. This apparent contradiction can be explained by the transient nature of the response. The rise in MDH1–CIT1 interaction following ETC inhibition was transient, suggesting that it does not represent steady-state changes in respiratory activity. Instead, it is more likely linked to acute changes in the mitochondrial matrix microenvironment. Notably, the timing of the increased interaction coincided with changes in matrix pH, supporting a role for pH-dependent regulation (see below). These findings align with our model, which posits that the MDH1–CIT1 interaction is controlled by microenvironmental changes accompanying shifts in respiration. In the case of ETC inhibition, transient perturbations of the matrix microenvironment appear to be disconnected from steady-state respiratory output, thereby promoting MDH1–CIT1 interaction despite overall inhibition of respiration.

We also investigated the molecular mechanisms regulating MDH1-CIT1 complex dynamics. We previously reported that protein conformation changes induced by the solution pH and allosteric regulators affect porcine MDH-CS complex interaction in vitro (Omini et al., 2021). The recombinant yeast MDH1 and CIT1 showed similar responses to the porcine enzymes; MDH1-CIT1 affinity was higher in low pH and in the presence of upstream TCA cycle intermediates (malate and fumarate) but disrupted in the presence of reaction product (citrate; Figure 5). These factors can affect the TCA cycle metabolon formation in vivo. The relationship between these factors and the MDH1-CIT1 interaction observed in this study is summarized in Figure 6A.

We observed an enhanced MDH1-CIT1 interaction under conditions that lower mitochondrial matrix pH in vivo. The mitochondrial matrix pH decreased after adding acetate, corresponding to the enhanced MDH1-CIT1 interaction (Figure 3 A, D). The time courses of the temporal increase in MDH1-CIT1 interaction and pH decrease were inversely related following the complex III and IV inhibitions (Figure 4B, C, E, F; Figure 6A). The decrease in the pH from 7.5 to 6.0 ranges is

376 remarkable since the K_d of MDH1-CIT1 association decreases by an order of magnitude within
377 this pH range (Figure 5A). The mitochondrial matrix acidification under respiratory conditions
378 likely favors the MDH1-CIT1 interaction. On the other hand, the mitochondria matrix pH was
379 maintained around 7.2 in the presence of glucose (Figure 2D), which likely weakens the MDH1-
380 CIT1 complex interaction. These results indicate that mitochondrial matrix pH, which is related to
381 proton transport activity by the ETC, can stabilize or destabilize the MDH1-CIT1 complex, thereby
382 regulating the MDH1-CIT1 interaction in response to respiratory activity (Figure 6B). Enhancing
383 the MDH1-CIT1 interaction with the uncoupler CCCP (Figure 4 – figure supplement) also
384 supports the prominent effect of pH.
385
386 Nevertheless, mitochondrial pH may influence the MDH1-CIT1 association, but it is not always
387 the predominant factor regulating the interaction. The observed changes in pH and interaction do
388 not consistently occur simultaneously following the Crabtree induction and acetate
389 supplementation (Figs 2 & 3). TCA cycle inhibitions reduce the MDH1-CIT1 interaction without
390 significantly affecting mitochondrial matrix pH (Figure 3B, C, E, F). These findings suggest that
391 mitochondrial matrix pH can be a contributing factor, either favoring or disfavoring the interaction,
392 rather than the primary regulator, which appears to be the direct induction and dissociation of the
393 MDH1-CIT1 complex.
394
395 Little evidence in this study supports a primary role for mitochondrial matrix redox state or ATP
396 levels in controlling MDH1–CIT1 interaction. Our in vitro analyses demonstrate that NAD(H) and
397 ATP can modulate MDH1–CIT1 interaction (Figure 5 - figure supplement 1B; Omini et al., 2021),
398 suggesting that these factors may contribute to complex dynamics. Although the lower matrix
399 ATP level following glucose supplementation (Figure 2D) and matrix reduction upon arsenite and
400 AOA-induced TCA cycle inhibition (Figure 3H&I) associated with decreased interaction (Figure 2A
401 and 3B&C), these relationships were not consistently observed across conditions (Figure 6A),
402 indicating that neither redox state nor ATP levels predict complex association in vivo. However,
403 we cannot rule out their contribution under specific metabolic contexts not captured in the current
404 study.
405
406 The TCA cycle intermediates and cofactors can also regulate the MDH1-CIT1 interaction,
407 considering their effects on the interaction in vitro (Omini et al., 2021). The yeast enzymes
408 showed responses to malate, α-ketoglutarate, succinate, and citrate (Figure 5B, Figure 5 – figure
409 supplement 1) similar to the enzymes of other organisms (Omini et al., 2021; Tompa et al., 1987;
410 Wu et al., 2015) , while fumarate is newly identified as an effector of the MDH-CS interaction.
411 Especially, fumarate, malate, and citrate showed significant influences on yeast enzymes (Figure
412 5B). Cellular levels of these effector metabolites significantly altered under the conditions tested
413 in this study (Figure 2E, 3M, 4M, 6A). Increased and decreased levels of malate and fumarate
414 following the TCA cycle and ETC inhibitions (Figure 3M&4M), respectively, are likely related to
415 the MDH1-CIT1 interaction since malate enhances the interaction (Figure 5D; Omini et al., 2021).
416 These results indicate the involvement of metabolite effectors, such as malate and fumarate, in
417 the regulation of the MDH1-CIT1 interaction (Figure 6). However, their precise effects must be
418 evaluated through site-specific, time-dependent perturbation and quantification of metabolite
419 levels in the mitochondrial matrix, as a whole-cell metabolite profile may not reflect the metabolite
420 concentrations that directly influence the complex association.
421
422 Aside from MDH1-CIT1 interaction dynamics, our results highlight the complex regulation of TCA
423 cycle metabolism. The activation and inhibition of respiratory activity resulted in diverse metabolic
424 phenotypes (Figure 6A, Supplementary Dataset 1), where intermediate levels did not simply
425 reflect overall pathway activity. This complexity stems from the distinct mechanisms of each
426 inhibitor, such as arsenite affecting α-ketoglutarate dehydrogenase and AOA disrupting the
427 malate-aspartate shuttle (Cavero et al., 2003; Eto et al., 1999; Lee et al., 2011; Liu and Butow,
428 2006), off-target effects of the inhibitors, and from the adaptive reorganization of intersecting
429 metabolic networks to bypass local blockades (Herrgård et al., 2008; Lehtinen et al., 2013;

430 Rogers et al., 2021). These diverse metabolic phenotypes allow us to assess the relationships
431 between metabolites and metabolon assembly independently of respiratory activity.
432
433 This study demonstrates that the TCA cycle MDH1-CIT1 multienzyme complex dynamically
434 interacts in response to the cellular respiratory status. Cues of cellular respiratory state may be
435 transmitted to the multienzyme complex, at least in part, by mitochondrial matrix
436 microenvironment and metabolite levels. In particular, mitochondrial matrix pH and malate and
437 fumarate levels likely have significant effects on the stability of the MDH1-CIT1 complex, since
438 these factors strongly influence complex affinity, and their in vivo changes coincide with complex
439 dynamics (Figure 6). However, none of these factors consistently correlates with the MDH1-CIT1
440 interaction (Figure 6A), suggesting that none of them is a predominant regulator, but multiple
441 factors work together in a cooperative manner to regulate the formation of the multienzyme
442 complex. This coordinated regulation probably serves to fine-tune the flux of the TCA cycle,
443 allowing it to adapt efficiently to varying metabolic demands and maintain cellular homeostasis.
444 Although we focused on allosteric regulators in this study, further factors are potentially involved
445 in the MDH1-CIT1 complex regulation. For example, 44 and 33 post-translational modifications
446 have been identified in CIT1 and MDH1, respectively (Bhagwat et al., 2021; Henriksen et al.,
447 2012; Holt et al., 2009; Lanz et al., 2021; Reinders et al., 2007; Swaney et al., 2013; Weinert et
448 al., 2013), some of which likely affect the MDH1-CIT1 complex affinity. Various scaffolding
449 molecules, such as long noncoding RNAs, lipid layers, and scaffolding proteins, have been
450 shown to stabilize the multienzyme complexes in other systems (Zhu et al., 2022). Future studies
451 should investigate the effects of these factors to understand the regulatory mechanisms for
452 MDH1-CIT1 interaction.
453
454 Changes in environmental conditions and nutrient availability occur swiftly, and a corresponding
455 change in metabolic flux must occur at a similar rate for the successful adaptation of living cells.
456 Dynamic metabolons can be a system to regulate and fine-tune metabolic network flux quickly,
457 allowing cells to maintain metabolic homeostasis in rapidly fluctuating environments (Obata,
458 2019). Considering the thermodynamic unfavorability of the forward MDH reaction and that
459 substrate channeling overcomes this thermodynamic barrier in vitro, the MDH1-CIT1 complex
460 formation likely enhances the forward TCA cycle flux (Bulutoglu et al., 2016; Fukuda et al., 2008;
461 Sweetlove et al., 2010). The dynamic assembly of the metabolon probably provides fine-tuning of
462 TCA cycle activity in response to respiratory demand. While the present study delineates the
463 environmental and metabolic factors governing this dynamic assembly, future studies utilizing
464 targeted genetic tools to independently modulate specific variables will be critical for dissecting
465 the contributions of individual regulatory factors in vivo. Further studies assessing the impacts of
466 metabolon formation on metabolic pathway flux in living cells are essential to understand the
467 functions of metabolons in metabolic network regulation. Elucidating the regulatory system of the
468 TCA cycle metabolon can lead to a novel strategy to manipulate the TCA cycle flux in metabolic
469 engineering to achieve efficient industrial production of various molecules requiring TCA cycle
470 intermediates as substrates or to control the Warburg effect to suppress cancer cells.
471
472 **Materials and Methods**
473 **Strains, media, and culture conditions**
474 *Saccharomyces cerevisiae* BY4741 (MATa his3Δ1 leu2Δ0 met15Δ0 ura3Δ0) was used as the
475 background strain. Cells were grown in synthetic complete medium (SD) containing 0.67% yeast
476 nitrogen base lacking amino acids (Research Products International, Mt. Prospect, IL, USA) with
477 2% w/v D-raffinose and 1% amino acid complete drop-out mix. The complete amino acid drop-out
478 mix was replaced with the amino acid drop-out mix lacking leucine for GoAteam expressing cells
479 or the amino acid drop-out mix lacking uracil for RoGFP and pHluorin expressing cells. Cell
480 growth cultures were incubated with shaking at 220 rpm at 28°C in an incubator shaker. Cell
481 cultures were grown to exponential phase with an OD_{600}=0.5 to 1.0 in all analyses.
482
483 **Oxygen consumption rate measurement**

484 Oxygen consumption was measured using a Clark-type electrode (Oxygraph, Hansatech
485 Instruments, Norfolk, UK) as described previously (Agrimi et al., 2011). Cells were grown to
486 exponential phase OD_{600}=0.5, harvested, centrifuged at 3,000 x *g* for 5 min at 4°C, and
487 resuspended in growth medium to obtain a density of OD_{600}=5.0. A total of 1 ml reaction volume
488 consisting of equal parts of 445 µl cell culture, 445 µl growth media, and 10 µl of each inhibitor
489 was added to the oxygraph chamber. Sodium malonate (20 mM), antimycin A (10 µM), sodium
490 cyanide (0.5 mM), and oligomycin (1 mM) were used as specific inhibitors of electron transport
491 chain complex II, III, IV, and V, respectively. The change in oxygen concentration was followed
492 subsequently. Oxygen consumption rates were determined before and after the addition of each
493 inhibitor from the slope of a plot of O_2 concentration versus time. All measurements were
494 conducted in triplicates.
495
496 **Generation of the *Saccharomyces cerevisiae* reporter strains with tagged MDH1 and CIT1**
497 The NanoBiT split NanoLUC luciferase complementation system (Dixon et al., 2016) was adopted
498 to monitor MDH1-CIT1 interaction in yeast cells. The yeast lines expressing MDH1 and CIT1
499 proteins fused with the small (SmBiT) and large (LgBiT) NanoBiT subunits, respectively, were
500 generated by inserting the yeast codon-optimized tag-coding sequences into the BY4741 genome
501 following the scarless C-terminal tagging procedure (Landgraf et al., 2016). The full-length
502 NanoLUC, LgBiT, and SmBiT coding sequences were integrated to direct downstream of the
503 Mdh1 (chrIV:3300230) and Cit1 (chrX:303993) genes on the BY4741 genome for C-terminal
504 fusion. The LgBiT and SmBiT sequences include flexible linkers (ACKIPNDLKQKVMNH; (Hu et
505 al., 2002)) with HA and cMyc epitope sequences, respectively, for immunological detections.
506 Details of the vector construction procedure, primers, and vectors are described in the
507 Supplementary Method.
508
509 Briefly, we generated the plasmids with integration cassettes composed of the linker, 5' half of
510 tag-coding sequence, URA3 selection marker, and 3' half of tag-coding sequence in this order
511 using the Golden Braid technology (Sarrion-Perdigones et al., 2013). The halves of the tag-
512 coding sequences have an overlapping sequence. The integration cassettes were amplified by
513 PCR using the primers with around 40 bases 5' extension with sequences homologous to the
514 franking region of the tag insertion sites. BY4741 cells were transformed with the purified PCR
515 products to insert the cassettes into the target sites directly downstream of the Mdh1 and Cit1
516 genes by homologous recombination due to the 5' extension of the primers. The transformants
517 were selected on uracil-deficient plates. To pop-out the URA3 marker and reconstruct NanoLUC
518 and NanoBiT subunits, the transformants were cultured overnight in uracil-containing YPD media.
519 The URA3 gene was excluded from the genome by recombination based on the overlapping
520 sequences in the cassette. The cell suspension was spread on SD plates containing 1 mg ml^{-1} 5-
521 fluoroorotic acid (5-FOA) to select the cell lines without the URA3 gene. SmBiT was initially fused
522 with the Mdh1 gene, and the resulting strain was further transformed to fuse LgBiT with Cit1
523 (MDH1/CIT1-BiT strain). Another strain expressing MDH1 fused with full-length NanoLUC
524 luciferase was also generated following the same procedure to monitor MDH1 protein levels
525 (MDH1-nLUC strain).
526
527 **In vivo MDH1-CIT1 interaction measurement**
528 The MDH1/CIT1-BiT strain expressing MDH1 and CIT1 enzymes tagged with split halves of
529 luciferase enzyme was grown to OD_{600} = 0.35-0.45. Cells were collected and resuspended to
530 obtain a cell density of OD_{600}=2.0 in fresh SD-Raff media. Each sample consisted of 80 µl of
531 media, 10 µl of cells, and 10 µl of 50x furimazine luciferase substrate (Promega, Madison, WI,
532 USA). The luminescence signal was measured every five min with a microplate reader
533 (CLARIOSTAR Plus, BMG LABTECH, Ortenberg, Germany) at 28°C with 200 rpm shaking at the
534 beginning of each cycle. Baseline luminescence was measured for 20 min before the treatment
535 was applied. The time-dependent luminescence was measured for an additional 80 min after
536 treatment. Relative luminescence Unit (RLU) was calculated by normalizing the luciferase signals
537 by the average signals during three pre-treatment time points. The protein levels of MDH1 and
538 CIT1 were assessed using yeast lines expressing these proteins tagged with full-length NanoLUC

539 luciferase. Using the luminescence data of these relative protein levels, we calculated normalized
540 interaction index by dividing the NanoBiT interaction signal by the product of the relative
541 abundances of both proteins:

542 $$Normalized\ Interaction\ Index = \frac{NanoBiT}{MDH1 * CIT1}$$

543 In this formula, NanoBiT, MDH1, and CIT1 are the relative luminescence levels at each time
544 point.
545
546 **Western blotting**
547 Cells were grown to OD_{600}=0.5 and cell pellet was collected. Cells were first pretreated with 2 M
548 LiAc and 0.4 M NaOH to permeabilize the cells and then treated with SDS-PAGE sample buffer
549 to extract proteins according to the method described by Zhang et al. (Zhang et al., 2011). The
550 cell lysate was centrifuged at 27,000 x *g* for 10 min at 4°C and the proteins were detected by
551 SDS-PAGE and western blotting following the method described previously (Rajasekaran et al.,
552 2022). cMyc Tag Monoclonal Antibody (MA1213161MG, Thermo Scientific) and HA Tag
553 Monoclonal Antibody (LSG26183, Thermo Fisher Scientific) were used as primary antibodies to
554 detect MDH1 and CIT1, respectively. DLD1 antibody generated by S. Claypool laboratory at the
555 Johns Hopkins University (Baile et al., 2013), and PGK1 Monoclonal Antibody (Invitrogen
556 459250, Thermo Fisher Scientific) was used to detect phosphoglycerate kinase as a
557 housekeeping protein and internal standard.
558
559 **In vitro MDH1-CIT1 interaction measurement**
560 The recombinant MDH1 and CIT1 were produced accordingsuw to the method described in the
561 Supplementary Methods. The interaction between recombinant MDH1 and CIT1 enzymes were
562 analyzed by microscale thermophoresis (MST) according to the method described by Omini et al.
563 (Omini et al., 2021) with slight modifications. Base MST buffer contained 50 mM Tris-HCL (pH 8),
564 150 mM NaCl, 10 mM $MgCl_2$, 5 mM DTT, and 0.05% Tween-20. Recombinant MDH1 (10 μM)
565 was labeled with Protein Labeling Kit RED-NHS 2nd Generation (NanoTemper, München,
566 Germany) and used as the target. CIT1 was used as the ligand. Two-times serial dilution of 80
567 μM CIT1 was conducted for 16 concentrations. A total of 10 μL of CIT1, 10 μL MST buffer, and 10
568 μL labeled MDH1 were mixed and loaded to Monolith NT.115 Capillaries (NanoTemper).
569 Capillaries were incubated at room temperature for 1 min, and the interaction was analyzed by
570 MST using Monolith NT.115 (NanoTemper). To test the effect of pH on MDH1-CIT1 interaction,
571 50 mM tris buffers with pH 6.0, 7.5, and 8.0 were prepared and used as the MST buffer for
572 sample preparation. To test the effect of reducing environment on interaction, various
573 concentrations (5 mM, 2.5 mM, 1.25 mM) of DTT were prepared with the MST buffer and used for
574 sample preparation. To test the effect of ATP level on interaction, an MST buffer containing
575 different concentrations of ATP (5 mM, 2.5 mM, 1.25 mM) was made and used for sample
576 preparation. To test the effect of metabolite availability on the interaction, MST buffer containing
577 respective metabolites at 10 mM concentration was made and used for sample preparation and
578 experiments.
579
580 **Enzyme activity assays**
581 Cells were grown to an exponential phase with OD_{600} of 0.5, and 2 ml of the cells were harvested
582 for enzyme activity assay. Yeast cell lysates were prepared by disruption with glass beads as
583 described previously (Mukherjee et al., 2020), with the lysis buffer omitted butylhydroxytoluene.
584 The protein concentration of the lysate was determined using Pierce™ BCA Protein Assay Kit
585 (Thermo Fischer Scientific). CS activity was determined using a method described previously
586 (Srere, 1969) that measures free thiols by coupling the citrate synthase reaction to thiol reaction
587 with 5, 5'-dithiobis-(2-nitrobenzoate) (DTNB). The CS enzyme activity assay mixture contained
588 154 μL of distilled water, 20 μL of 1 mM DTNB, and 6 μL of 10 mM acetyl CoA. The citrate
589 synthase reaction was initiated by the addition of 10 μL of 10 mM oxaloacetate. The absorption at
590 412 nm was followed to measure citrate synthase activity. MDH activity assay mixture contained

591 50 mM TES (pH 7.2), 5 mM $MgCl_2$, 0.2 mM NADH, and 0.05% Triton X100. To obtain a total
592 reaction volume of 300 µL, 285 µL of the assay mixture and 5 µL cell lysate were added to the
593 wells, and the reaction was initiated with 10 µL of 30 mM oxaloacetate. Reduction of NADH was
594 followed at 340 nm to determine MDH enzyme activity. Enzyme activity was measured using a
595 microplate reader absorbance function (CLARIOSTAR Plus, BMG LABTECH).
596
597 **Metabolite profiling**
598 Yeast cells were grown to the exponential phase (OD_{600}~0.5), and treatments were applied and
599 incubated for the time described in the figure legends. Cellular metabolites were extracted
600 following the protocol described by Obata et al. (Obata et al., 2013). The cells in 1 mL culture
601 were harvested by vacuum filtration using a membrane filter (0.45 µm HV Durapore 25 mm
602 diameter; MilliporeSigma, Burlington, MA, USA). The filter was put into a 2 mL microcentrifuge
603 tube, flash-frozen in liquid nitrogen, and stored at −80°C. The metabolites were extracted from
604 the filtered cells with methanol: water: chloroform, and 50 µL aliquot was dried down by vacuum
605 centrifugation. Dried metabolites were derivatized with methoxyamine hydrochloride in pyridine
606 and further trimethylsylilated by N-Methyl-N-(trimethylsilyl) trifluoroacetamide (MilliporeSigma).
607 Derivatized samples were analyzed by 7200 GC-QTOF system (Agilent, Santa Clara, CA, USA)
608 exactly as described in Wase et al. (Wase et al., 2022). Each metabolite's peak height was
609 normalized by the peak height of the internal standard (ribitol) to represent relative levels of
610 metabolite.
611
612 **Expression of mitochondrial biosensors**
613 The pH, redox state, and ATP levels in the mitochondrial matrix were measured using the mito-
614 Go Ateam2, mito-ROGFP1, and pHluorin (pAG416-COX4-pHluorin, URA selection marker)
615 fluorescence biosensors, respectively, specifically localizing in the mitochondrial matrix. The mito-
616 Go Ateam2 (p415-GPDpro-mito GO ATeam) and mito-roGFP1 (p416-GPDpro-mito roGFP)
617 encoding plasmids (Vevea et al., 2013) were generous gifts from Dr. Liza Pon at Department of
618 Pathology and Cell Biology, Columbia University. The pHluorin encoded plasmid (pAG416-COX4-
619 pHluorin;(Ayer et al., 2013)) was a generous gift from Dr. Anita Ayer at the University of New South
620 Wales, Sydney, Australia. The plasmids encoding these biosensors were transformed into split-
621 Luc tagged MDH1/CIT1 strain using the lithium acetate method (Chen et al., 1992). The p416-
622 GPDpro-mito roGFP and pAG416-COX4-pHluorin harboring cells were selected on URA- media,
623 and the cells with p415-GPDpro-mito GO ATeam were selected on Leu- media.
624
625 The localization of biosensors within the mitochondria was confirmed by confocal microscopy.
626 Cells were grown in SD selection media to OD_{600}=0.50. Cells were stained with MitoTracker Deep
627 Red FM (ThermoFisher Scientific) in a 100 nM dye solution for 30 min with shaking at 28 °C to
628 visualize the mitochondria. The stained cells were resuspended in fresh 10 mM HEPES buffer
629 (pH 7.4) with 2% raffinose to obtain a final concentration of OD_{600}=10. Confocal imaging was
630 performed on an A1R-Ti2 Confocal Laser Scanning Microscope (Nikon, Tokyo, Japan) with a
631 Plan Apo 60x 1.40 Oil lens 0.17 WD 0.13 (Nikon) and a 2x digital zoom for a total magnification of
632 1200x. Brightfield and fluorescent images were captured. Imaging was done sequentially with
633 excitation at 405 nm and emission at 425-475 nm for pHluorin and mito-roGFP1, excitation at 488
634 nm and emission at 500-550 nm for mito-GoAteam2, and excitation at 640 nm and emission at
635 663-738 nm for MitoTracker. Images were collected with NIS Elements software (Nikon) and
636 processed with ImageJ analysis software (Vevea et al., 2013).
637
638 **Measurement of redox state, pH, and ATP level in the mitochondrial matrix**
639 Cells expressing pHluorin, mito-roGFP1, and mito-GoAteam2 were grown to OD_{600}=0.50 in their
640 respective selection media. Cells were prepared for fluorescence measurement according to the
641 method described by Morgan *et al* (Morgan et al., 2011). Time-based fluorescence intensity was
642 measured using a microplate reader (CLARIOSTAR Plus, BMG LABTECH) at 28°C with shaking
643 at 200 rpm with 20 min of baseline measurement before treatments. In all experiments, the
644 strains harboring empty vectors were grown simultaneously as a reference for background

645 fluorescence at the different excitation wavelengths. Background fluorescence was subtracted
646 from fluorescence intensity from cells expressing biosensors.
647
648 For the pH measurement, the ratio of emission intensity at 510 nm resulting from excitation of
649 pHluorin at 390 nm and 470 nm was calculated (R390/470) using pHluorin expressing strain. The
650 mitochondrial matrix pH was calculated from the R390/470 ratio using a calibration curve
651 generated according to the method described by Orij *et al* (Orij et al., 2009). Briefly, pHluorin-
652 expressing cells were permeabilized by resuspension in PBS containing 100 µg ml-1 digitonin for
653 10 min and washed with PBS. Cells were resuspended in citric acid/Na2HPO4 buffer of pH
654 values ranging from 5.0 to 9.0. The ratio of pHluorin emission at 510 nm upon excitation at 390
655 and 470 nm (R390/470) was plotted against buffer pH to obtain a calibration curve.
656
657 The mitochondrial matrix redox state was measured using mito-roGFP1 expressing strain. The
658 ratio of emission intensity at 510 nm from excitation at 365 nm and 470 nm (R470/365) was
659 measured. Mito-roGFP1 in situ calibration was performed following the method described by
660 (Vevea et al., 2013). Digitonin-treated mito-roGFP1 expressing cells were incubated in 0, 5, and
661 10 mM H_2O_2 and DTT for 20 min at 28°C with shaking at 200 rpm. The R470/365 was plotted
662 against the redox potential of the solutions calculated using the formula described previously
663 (Morgan et al., 2011).
664
665 Relative ATP level was determined by measuring the ratio of the emission intensity of mito-
666 GoAteam2 at 510 nm and 560 nm with excitation at 470 nm (R560/510). The ATP levels were
667 analyzed as the relative value without calibration to absolute concentrations.
668
669 **Statistical Analysis.**
670 The differences between the control and test samples were evaluated by a two-tailed unpaired
671 Student's *t*-test. $p < 0.05$ was considered a statistically significant difference. For the time course
672 data, the test was applied at each time point. All data was obtained from triplicated independent
673 experiments.
674
675 **Acknowledgments**
676 This study is supported by the NSF CAREER Award to TO under Grant No. 1845451. Dr. Liza
677 Pon at Columbia University kindly gifted us the mito-Go Ateam2 and mito-ROGFP1 biosensors,
678 and Dr. Anita Ayer at the University of New South Wales, Sydney, Australia, gifted us the
679 pHluorin mitochondrial biosensor. Dr. Oleh Khalimonchuk at the University of Nebraska-Lincoln
680 provided us with the anti-DLD1 antibody. The Microscopy work assisted by Terri Fangman was
681 carried out at the Microscopy Research Core Facility of the Center for Biotechnology at the
682 University of Nebraska-Lincoln, which is partially funded by the Nebraska Center for Integrated
683 Biomolecular Communication COBRE grant (P20 GM113126 and NIGMS) and the Nebraska
684 Research Initiative. This paper is based on a dissertation submitted by Joy Omini to fulfill the
685 requirements for the degree of Doctor of Philosophy, University of Nebraska-Lincoln (Omini,
686 2024).
687
688 **References**
689 Agrimi G, Brambilla L, Frascotti G, Pisano I, Porro D, Vai M, Palmieri L. 2011. Deletion or
690 Overexpression of Mitochondrial NAD + Carriers in Saccharomyces cerevisiae Alters
691 Cellular NAD and ATP Contents and Affects Mitochondrial Metabolism and the Rate of
692 Glycolysis. Applied and Environmental Microbiology **77**:2239–2246. DOI:
693 https://doi.org/10.1128/AEM.01703-10
694 Ahmadzadeh M, Horng A, Colombini M. 1996. The control of mitochondrial respiration in yeast:
695 A possible role of the outer mitochondrial membrane. Cell Biochemistry and Function
696 **14**:201–208. DOI: https://doi.org/10.1002/cbf.673

697 Ayer A, Sanwald J, Pillay BA, Meyer AJ, Perrone GG, Dawes IW. 2013. Distinct Redox Regulation
698 in Sub-Cellular Compartments in Response to Various Stress Conditions in
699 Saccharomyces cerevisiae. PLOS ONE **8**:e65240. DOI:
700 https://doi.org/10.1371/journal.pone.0065240
701 Baile MG, Whited K, Claypool SM. 2013. Deacylation on the matrix side of the mitochondrial
702 inner membrane regulates cardiolipin remodeling. Molecular Biology of the Cell
703 **24**:2008–2020. DOI: https://doi.org/10.1091/mbc.e13-03-0121
704 Beeckmans S. 1984. Some structural and regulatory aspects of citrate synthase. International
705 Journal of Biochemistry **16**:341–351. DOI: https://doi.org/10.1016/0020-
706 711X(84)90131-9
707 Beeckmans S, Kanarek L. 1981. Demonstration of Physical Interactions between Consecutive
708 Enzymes of the Citric Acid Cycle and of the Aspartate-Malate Shuttle. European Journal
709 of Biochemistry **117**:527–535. DOI: https://doi.org/10.1111/j.1432-1033.1981.tb06369.x
710 Bhagwat NR, Owens SN, Ito M, Boinapalli J V, Poa P, Ditzel A, Kopparapu S, Mahalawat M, Davies
711 OR, Collins SR, Johnson JR, Krogan NJ, Hunter N. 2021. SUMO is a pervasive regulator of
712 meiosis. eLife **10**. DOI: https://doi.org/10.7554/eLife.57720
713 Borst P. 2020. The malate–aspartate shuttle (Borst cycle): How it started and developed into a
714 major metabolic pathway. IUBMB Life **72**:2241–2259. DOI:
715 https://doi.org/10.1002/iub.2367
716 Bulutoglu B, Garcia KE, Wu F, Minteer SD, Banta S. 2016. Direct Evidence for Metabolon
717 Formation and Substrate Channeling in Recombinant TCA Cycle Enzymes. ACS Chemical
718 Biology **11**:2847–2853. DOI: https://doi.org/10.1021/acschembio.6b00523, PMID:
719 27556423
720 Causton HC, Ren B, Koh SS, Harbison CT, Kanin E, Jennings EG, Lee TI, True HL, Lander ES, Young
721 RA. 2001. Remodeling of Yeast Genome Expression in Response to Environmental
722 Changes. Molecular Biology of the Cell **12**:323–337. DOI:
723 https://doi.org/10.1091/mbc.12.2.323
724 Cavero S, Vozza A, Del Arco A, Palmieri L, Villa A, Blanco E, Runswick MJ, Walker JE, Cerdán S,
725 Palmieri F, Satrústegui J. 2003. Identification and metabolic role of the mitochondrial
726 aspartate-glutamate transporter in Saccharomyces cerevisiae. Molecular Microbiology
727 **50**:1257–1269. DOI: https://doi.org/10.1046/j.1365-2958.2003.03742.x
728 Chen D-C, Yang B-C, Kuo T-T. 1992. One-step transformation of yeast in stationary phase.
729 Current Genetics **21**:83–84. DOI: https://doi.org/10.1007/BF00318659
730 Diaz-Ruiz R, Rigoulet M, Devin A. 2011. The Warburg and Crabtree effects: On the origin of
731 cancer cell energy metabolism and of yeast glucose repression. Biochimica et Biophysica
732 Acta (BBA) - Bioenergetics **1807**:568–576. DOI:
733 https://doi.org/10.1016/j.bbabio.2010.08.010
734 Dixon AS, Schwinn MK, Hall MP, Zimmerman K, Otto P, Lubben TH, Butler BL, Binkowski BF,
735 Machleidt T, Kirkland TA, Wood MG, Eggers CT, Encell LP, Wood KV. 2016. NanoLuc
736 Complementation Reporter Optimized for Accurate Measurement of Protein
737 Interactions in Cells. ACS Chemical Biology **11**:400–408. DOI:
738 https://doi.org/10.1021/acschembio.5b00753
739 Eto K, Tsubamoto Y, Terauchi Y, Sugiyama T, Kishimoto T, Takahashi N, Yamauchi N, Kubota N,
740 Murayama S, Aizawa T, Akanuma Y, Aizawa S, Kasai H, Yazaki Y, Kadowaki T. 1999. Role
741 of NADH Shuttle System in Glucose-Induced Activation of Mitochondrial Metabolism
742 and Insulin Secretion. Science **283**:981–985. DOI:
743 https://doi.org/10.1126/science.283.5404.981

744 Fukuda J, Tsujimura S, Kano K. 2008. Coulometric bioelectrocatalytic reactions based on NAD-
745 dependent dehydrogenases in tricarboxylic acid cycle. Electrochimica Acta **54**:328–333.
746 DOI: https://doi.org/10.1016/J.ELECTACTA.2008.07.071
747 Gancedo JM. 1998. Yeast Carbon Catabolite Repression. Microbiology and Molecular Biology
748 Reviews **62**:334–361. DOI: https://doi.org/10.1128/MMBR.62.2.334-361.1998
749 Gerstmeir R, Wendisch VF, Schnicke S, Ruan H, Farwick M, Reinscheid D, Eikmanns BJ. 2003.
750 Acetate metabolism and its regulation in Corynebacterium glutamicum. Journal of
751 Biotechnology **104**:99–122. DOI: https://doi.org/10.1016/S0168-1656(03)00167-6
752 Guaragnella N, Ždralević M, Lattanzio P, Marzulli D, Pracheil T, Liu Z, Passarella S, Marra E,
753 Giannattasio S. 2013. Yeast growth in raffinose results in resistance to acetic-acid
754 induced programmed cell death mostly due to the activation of the mitochondrial
755 retrograde pathway. Biochimica et Biophysica Acta (BBA) - Molecular Cell Research
756 **1833**:2765–2774. DOI: https://doi.org/10.1016/j.bbamcr.2013.07.017
757 Halper LA, Srere PA. 1977. Interaction between citrate synthase and mitochondrial malate
758 dehydrogenase in the presence of polyethylene glycol. Archives of biochemistry and
759 biophysics **184**:529–534. PMID: 563705
760 Henriksen P, Wagner SA, Weinert BT, Sharma S, Bačinskaja G, Rehman M, Juffer AH, Walther TC,
761 Lisby M, Choudhary C. 2012. Proteome-wide Analysis of Lysine Acetylation Suggests its
762 Broad Regulatory Scope in Saccharomyces cerevisiae. Molecular & Cellular Proteomics
763 **11**:1510–1522. DOI: https://doi.org/10.1074/mcp.M112.017251
764 Herrgård MJ, Swainston N, Dobson P, Dunn WB, Arga KY, Arvas M, Blüthgen N, Borger S,
765 Costenoble R, Heinemann M, Hucka M, Le Novère N, Li P, Liebermeister W, Mo ML,
766 Oliveira AP, Petranovic D, Pettifer S, Simeonidis E, Smallbone K, Spasié I, Weichart D,
767 Brent R, Broomhead DS, Westerhoff HV, Kürdar B, Penttilä M, Klipp E, Palsson BØ, Sauer
768 U, Oliver SG, Mendes P, Nielsen J, Kell DB. 2008. A consensus yeast metabolic network
769 reconstruction obtained from a community approach to systems biology. Nature
770 Biotechnology **26**:1155–1160. DOI: https://doi.org/10.1038/nbt1492
771 Holt LJ, Tuch BB, Villén J, Johnson AD, Gygi SP, Morgan DO. 2009. Global Analysis of Cdk1
772 Substrate Phosphorylation Sites Provides Insights into Evolution. Science **325**:1682–
773 1686. DOI: https://doi.org/10.1126/science.1172867
774 Hu C-D, Chinenov Y, Kerppola TK. 2002. Visualization of interactions among bZIP and Rel family
775 proteins in living cells using bimolecular fluorescence complementation. Molecular cell
776 **9**:789–98. PMID: 11983170
777 Huang YM, Huber GA, Wang N, Minteer SD, Mccammon JA. 2018. Brownian dynamic study of an
778 enzyme metabolon in the TCA cycle: Substrate kinetics and channeling. Protein Science
779 **27**:463–471. DOI: https://doi.org/10.1002/pro.3338
780 Klein CJL, Olsson L, Nielsen J. 1998. Glucose control in Saccharomyces cerevisiae: the role of
781 MIG1 in metabolic functions. Microbiology **144**:13–24. DOI:
782 https://doi.org/10.1099/00221287-144-1-13
783 Landgraf D, Huh D, Hallacli E, Lindquist S. 2016. Scarless Gene Tagging with One-Step
784 Transformation and Two-Step Selection in Saccharomyces cerevisiae and
785 Schizosaccharomyces pombe. PLOS ONE **11**:e0163950. DOI:
786 https://doi.org/10.1371/journal.pone.0163950
787 Lanz MC, Yugandhar K, Gupta S, Sanford EJ, Faça VM, Vega S, Joiner AMN, Fromme JC, Yu H,
788 Smolka MB. 2021. In-depth and 3-dimensional exploration of the budding yeast
789 phosphoproteome. EMBO reports **22**. DOI: https://doi.org/10.15252/embr.202051121

790 Lee YJ, Jang JW, Kim KJ, Maeng PJ. 2011. TCA cycle-independent acetate metabolism via the
791 glyoxylate cycle in Saccharomyces cerevisiae. Yeast **28**:153–166. DOI:
792 https://doi.org/10.1002/yea.1828
793 Lehtinen S, Marsellach FX, Codlin S, Schmidt A, Clément-Ziza M, Beyer A, Bähler J, Orengo C,
794 Pancaldi V. 2013. Stress induces remodelling of yeast interaction and co-expression
795 networks. Molecular BioSystems **9**:1697–1707. DOI:
796 https://doi.org/10.1039/C3MB25548D
797 Litsios A, Ortega ÁD, Wit EC, Heinemann M. 2018. Metabolic-flux dependent regulation of
798 microbial physiology. Current Opinion in Microbiology **42**:71–78. DOI:
799 https://doi.org/10.1016/j.mib.2017.10.029
800 Liu Z, Butow RA. 2006. Mitochondrial Retrograde Signaling. Annual Review of Genetics **40**:159–
801 185. DOI: https://doi.org/10.1146/annurev.genet.40.110405.090613
802 Meyer FM, Gerwig J, Hammer E, Herzberg C, Commichau FM, Völker U, Stülke J. 2011. Physical
803 interactions between tricarboxylic acid cycle enzymes in Bacillus subtilis: Evidence for a
804 metabolon. Metabolic Engineering **13**:18–27. DOI:
805 https://doi.org/10.1016/j.ymben.2010.10.001, PMID: 20933603
806 Molinié T, Cougouilles E, David C, Cahoreau E, Portais J-C, Mourier A. 2022. MDH2 produced
807 OAA is a metabolic switch rewiring the fuelling of respiratory chain and TCA cycle.
808 Biochimica et Biophysica Acta (BBA) - Bioenergetics **1863**:148532. DOI:
809 https://doi.org/10.1016/j.bbabio.2022.148532
810 Morgan B, Sobotta MC, Dick TP. 2011. Measuring EGSH and H2O2 with roGFP2-based redox
811 probes. Free Radical Biology and Medicine **51**:1943–1951. DOI:
812 https://doi.org/10.1016/j.freeradbiomed.2011.08.035
813 Morgunov I, Srere PA. 1998. Interaction between citrate synthase and malate dehydrogenase:
814 Substrate channeling of oxaloacetate. Journal of Biological Chemistry **273**:29540–29544.
815 DOI: https://doi.org/10.1074/jbc.273.45.29540, PMID: 9792662
816 Mukherjee M, Nandi A, Chandra K, Saikia SK, Jana CK, Das N. 2020. Protein extraction from
817 Saccharomyces cerevisiae at different growth phases. Journal of Microbiological
818 Methods **172**:105906. DOI: https://doi.org/10.1016/j.mimet.2020.105906
819 Noor E, Bar-Even A, Flamholz A, Reznik E, Liebermeister W, Milo R. 2014. Pathway
820 thermodynamics highlights kinetic obstacles in central metabolism. PLoS computational
821 biology **10**:e1003483. DOI: https://doi.org/10.1371/journal.pcbi.1003483, PMID:
822 24586134
823 Obata T. 2020. Toward an evaluation of metabolite channeling in vivo. Current Opinion in
824 Biotechnology **64**:55–61. DOI: https://doi.org/10.1016/j.copbio.2019.09.013
825 Obata T. 2019. Metabolons in plant primary and secondary metabolism. Phytochemistry
826 Reviews **18**:1483–1507. DOI: https://doi.org/10.1007/s11101-019-09619-x
827 Obata T, Schoenefeld S, Krahnert I, Bergmann S, Scheffel A, Fernie A. 2013. Gas-
828 Chromatography Mass-Spectrometry (GC-MS) Based Metabolite Profiling Reveals
829 Mannitol as a Major Storage Carbohydrate in the Coccolithophorid Alga Emiliania
830 huxleyi. Metabolites **3**:168–184. DOI: https://doi.org/10.3390/metabo3010168
831 Omini J. 2024. Doctoral dissertation: Role of the Malate Dehydrogenase-Citrate Synthase
832 Metabolon in Metabolic Flux Regulation. University of Nebraska-Lincoln.
833 Omini J, Dele-Osibanjo T, Kim H, Zhang J, Obata T. 2024. Is the TCA cycle malate dehydrogenase-
834 citrate synthase metabolon an illusion? Essays in Biochemistry. DOI:
835 https://doi.org/10.1042/EBC20230084

836 Omini J, Wojciechowska I, Skirycz A, Moriyama H, Obata T. 2021. Association of the malate
837 dehydrogenase-citrate synthase metabolon is modulated by intermediates of the Krebs
838 tricarboxylic acid cycle. Scientific Reports **11**:18770. DOI:
839 https://doi.org/10.1038/s41598-021-98314-z, PMID: 34548590
840 Orij R, Postmus J, Ter Beek A, Brul S, Smits GJ. 2009. In vivo measurement of cytosolic and
841 mitochondrial pH using a pH-sensitive GFP derivative in Saccharomyces cerevisiae
842 reveals a relation between intracellular pH and growth. Microbiology **155**:268–278. DOI:
843 https://doi.org/10.1099/mic.0.022038-0
844 Orlandi I, Coppola D, Vai M. 2014. Rewiring yeast acetate metabolism through MPC1 loss of
845 function leads to mitochondrial damage and decreases chronological lifespan. Microbial
846 Cell **1**:393–405. DOI: https://doi.org/10.15698/mic2014.12.178
847 Pfeiffer T, Morley A. 2014. An evolutionary perspective on the Crabtree effect. Frontiers in
848 Molecular Biosciences **1**. DOI: https://doi.org/10.3389/fmolb.2014.00017
849 Polakis E, Bartley W. 1965. Changes in the enzyme activities of Saccharomyces cerevisiae during
850 aerobic growth on different carbon sources. Biochemical Journal **97**:284–297. DOI:
851 https://doi.org/10.1042/bj0970284
852 Rajasekaran S, Peterson PP, Liu Z, Robinson LC, Witt SN. 2022. α-synuclein inhibits Snx3-
853 retromer retrograde trafficking of the conserved membrane-bound proprotein
854 convertase Kex2 in the secretory pathway of Saccharomyces cerevisiae. Human
855 Molecular Genetics **31**:705–717. DOI: https://doi.org/10.1093/hmg/ddab284
856 Reinders J, Wagner K, Zahedi RP, Stojanovski D, Eyrich B, van der Laan M, Rehling P, Sickmann A,
857 Pfanner N, Meisinger C. 2007. Profiling Phosphoproteins of Yeast Mitochondria Reveals
858 a Role of Phosphorylation in Assembly of the ATP Synthase. Molecular & Cellular
859 Proteomics **6**:1896–1906. DOI: https://doi.org/10.1074/mcp.M700098-MCP200
860 Rep M, Reiser V, Gartner U, Thevelein JM, Hohmann S, Ammerer G, Ruis H. 1999. Osmotic
861 Stress-Induced Gene Expression in Saccharomyces cerevisiae Requires Msn1p and the
862 Novel Nuclear Factor Hot1p. Molecular and Cellular Biology **19**:5474–5485. DOI:
863 https://doi.org/10.1128/MCB.19.8.5474
864 Robinson JB, Inman L, Sumegi B, Srere PA. 1987. Further characterization of the Krebs
865 tricarboxylic acid cycle metabolon. The Journal of biological chemistry **262**:1786–1790.
866 PMID: 2433288
867 Rogers S, Hariri H, Wood NE, Speer NO, Henne WM. 2021. Glucose restriction drives spatial
868 reorganization of mevalonate metabolism. eLife **10**:e62591. DOI:
869 https://doi.org/10.7554/eLife.62591
870 Rolland F, Winderickx J, Thevelein JM. 2002. Glucose-sensing and -signalling mechanisms in
871 yeast. FEMS Yeast Research **2**:183–201. DOI: https://doi.org/10.1111/j.1567-
872 1364.2002.tb00084.x
873 Ronne H. 1995. Glucose repression in fungi. Trends in Genetics **11**:12–17. DOI:
874 https://doi.org/10.1016/S0168-9525(00)88980-5
875 Rosado CJ, Mijaljica D, Hatzinisiriou I, Prescott M, Devenish RJ. 2008. Rosella: A fluorescent pH-
876 biosensor for reporting vacuolar turnover of cytosol and organelles in yeast. Autophagy
877 **4**:205–213. DOI: https://doi.org/10.4161/auto.5331, PMID: 18094608
878 Santo-Domingo J, Demaurex N. 2012. The renaissance of mitochondrial pH. Journal of General
879 Physiology **139**:415–423. DOI: https://doi.org/10.1085/jgp.201110767
880 Sarrion-Perdigones A, Vazquez-Vilar M, Palaci J, Castelijns B, Forment J, Ziarsolo P, Blanca J,
881 Granell A, Orzaez D. 2013. GoldenBraid 2.0: A Comprehensive DNA Assembly

882 Framework for Plant Synthetic Biology. PLANT PHYSIOLOGY **162**:1618–1631. DOI:
883 https://doi.org/10.1104/pp.113.217661
884 Schüller H-J. 2003. Transcriptional control of nonfermentative metabolism in the yeast
885 Saccharomyces cerevisiae. Current Genetics **43**:139–160. DOI:
886 https://doi.org/10.1007/s00294-003-0381-8
887 Selivanov VA, Zeak JA, Roca J, Cascante M, Trucco M, Votyakova T V. 2008. The Role of External
888 and Matrix pH in Mitochondrial Reactive Oxygen Species Generation. Journal of
889 Biological Chemistry **283**:29292–29300. DOI: https://doi.org/10.1074/jbc.M801019200
890 Spivey HO, Ovádi J. 1999. Substrate channeling. Methods (San Diego, Calif.) **19**:306–321. DOI:
891 https://doi.org/10.1006/meth.1999.0858, PMID: 10527733
892 Srere PA. 1985. The metabolon. Trends in Biochemical Sciences **10**:109–110. DOI:
893 https://doi.org/10.1016/0968-0004(85)90266-X
894 Srere PA. 1969. [1] Citrate synthase. *Methods in Enzymology*. p. 3–11. DOI:
895 https://doi.org/10.1016/0076-6879(69)13005-0
896 Strittmatter CF. 1957. Adaptive Variation in the Level of Oxidative Activity in Saccharomyces
897 cerevisiae. Journal of General Microbiology **16**:169–183. DOI:
898 https://doi.org/10.1099/00221287-16-1-169
899 Sumegi B, Sherry AD, Malloy CR, Srere PA. 1993. Evidence for orientation-conserved transfer in
900 the TCA cycle in Saccharomyces cerevisiae: carbon-13 NMR studies. Biochemistry
901 **32**:12725–12729. DOI: https://doi.org/10.1021/bi00210a022
902 Swaney DL, Beltrao P, Starita L, Guo A, Rush J, Fields S, Krogan NJ, Villén J. 2013. Global analysis
903 of phosphorylation and ubiquitylation cross-talk in protein degradation. Nature
904 Methods **10**:676–682. DOI: https://doi.org/10.1038/nmeth.2519
905 Sweetlove LJ, Beard KFM, Nunes-Nesi A, Fernie AR, Ratcliffe RG. 2010. Not just a circle: Flux
906 modes in the plant TCA cycle. Trends in Plant Science **15**:462–470. DOI:
907 https://doi.org/10.1016/j.tplants.2010.05.006, PMID: 20554469
908 Thierie J, Penninckx M. 2010. Crabtree Effect. Encyclopedia of Industrial Biotechnology. DOI:
909 https://doi.org/10.1002/9780470054581.eib243
910 Tompa P, Batke J, Ovadi J, Welch GR, Srere PA. 1987. Quantitation of the interaction between
911 citrate synthase and malate dehydrogenase. Journal of Biological Chemistry **262**:6089–
912 6092. DOI: https://doi.org/10.1016/S0021-9258(18)45541-X
913 van Urk H, Schipper D, Breedveld GJ, Mak PR, Alexander Scheffers W, van Dijken JP. 1989.
914 Localization and kinetics of pyruvate-metabolizing enzymes in relation to aerobic
915 alcoholic fermentation in Saccharomyces cerevisiae CBS 8066 and Candida utilis CBS
916 621. Biochimica et Biophysica Acta (BBA) - General Subjects **992**:78–86. DOI:
917 https://doi.org/10.1016/0304-4165(89)90053-6
918 Vevea JD, Alessi Wolken DM, Swayne TC, White AB, Pon LA. 2013. Ratiometric Biosensors that
919 Measure Mitochondrial Redox State and ATP in Living Yeast Cells. Journal of Visualized
920 Experiments 1–12. DOI: https://doi.org/10.3791/50633, PMID: 23912244
921 Vilela-Moura A, Schuller D, Mendes-Faia A, Silva RD, Chaves SR, Sousa MJ, Côrte-Real M. 2011.
922 The impact of acetate metabolism on yeast fermentative performance and wine quality:
923 reduction of volatile acidity of grape musts and wines. Applied Microbiology and
924 Biotechnology **89**:271–280. DOI: https://doi.org/10.1007/s00253-010-2898-3
925 Wase N, Abshire N, Obata T. 2022. High-Throughput Profiling of Metabolic Phenotypes Using
926 High-Resolution GC-MS. . p. 235–260. DOI: https://doi.org/10.1007/978-1-0716-2537-
927 8_19

928 Weinert BT, Schölz C, Wagner SA, Iesmantavicius V, Su D, Daniel JA, Choudhary C. 2013. Lysine
929 Succinylation Is a Frequently Occurring Modification in Prokaryotes and Eukaryotes and
930 Extensively Overlaps with Acetylation. Cell Reports **4**:842–851. DOI:
931 https://doi.org/10.1016/j.celrep.2013.07.024
932 Wheeldon I, Minteer SD, Banta S, Barton SC, Atanassov P, Sigman M. 2016. Substrate
933 channelling as an approach to cascade reactions. Nature Chemistry **8**:299–309. DOI:
934 https://doi.org/10.1038/nchem.2459
935 Williamson JR, Cooper RH. 1980. Regulation of the citric acid cycle in mammalian systems. FEBS
936 Letters **117**:K73–K85. DOI: https://doi.org/10.1016/0014-5793(80)80572-2
937 Wu F, Minteer S. 2015. Krebs Cycle Metabolon: Structural Evidence of Substrate Channeling
938 Revealed by Cross-Linking and Mass Spectrometry. Angewandte Chemie International
939 Edition **54**:1851–1854. DOI: https://doi.org/10.1002/anie.201409336, PMID: 25537779
940 Wu F, Pelster LN, Minteer SD. 2015. Krebs cycle metabolon formation: metabolite concentration
941 gradient enhanced compartmentation of sequential enzymes. Chemical
942 Communications **51**:1244–1247. DOI: https://doi.org/10.1039/C4CC08702J
943 Yin X, Li J, Shin H, Du G, Liu L, Chen J. 2015. Metabolic engineering in the biotechnological
944 production of organic acids in the tricarboxylic acid cycle of microorganisms: Advances
945 and prospects. Biotechnology Advances **33**:830–841. DOI:
946 https://doi.org/10.1016/j.biotechadv.2015.04.006
947 Zhang T, Lei J, Yang H, Xu K, Wang R, Zhang Z. 2011. An improved method for whole protein
948 extraction from yeast Saccharomyces cerevisiae. Yeast **28**:795–798. DOI:
949 https://doi.org/10.1002/yea.1905
950 Zhang Y, Beard KFM, Swart C, Bergmann S, Krahnert I, Nikoloski Z, Graf A, Ratcliffe RG,
951 Sweetlove LJ, Fernie AR, Obata T. 2017. Protein-protein interactions and metabolite
952 channelling in the plant tricarboxylic acid cycle. Nature communications **8**:15212. DOI:
953 https://doi.org/10.1038/ncomms15212, PMID: 28508886
954 Zhang Y, Su M, Wang Z, Nielsen J, Liu Z. 2022. Rewiring regulation on respiro-fermentative
955 metabolism relieved Crabtree effects in Saccharomyces cerevisiae. Synthetic and
956 Systems Biotechnology **7**:1034–1043. DOI: https://doi.org/10.1016/j.synbio.2022.06.004
957 Zhu Y, Jin L, Shi R, Li J, Wang Y, Zhang L, Liang C-Z, Narayana VK, De Souza DP, Thorne RF, Zhang
958 LR, Zhang XD, Wu M. 2022. The long noncoding RNA glycoLINC assembles a lower
959 glycolytic metabolon to promote glycolysis. Molecular Cell **82**:542-554.e6. DOI:
960 https://doi.org/10.1016/j.molcel.2021.11.017
961
962
963

964 **Figures and Tables**
965

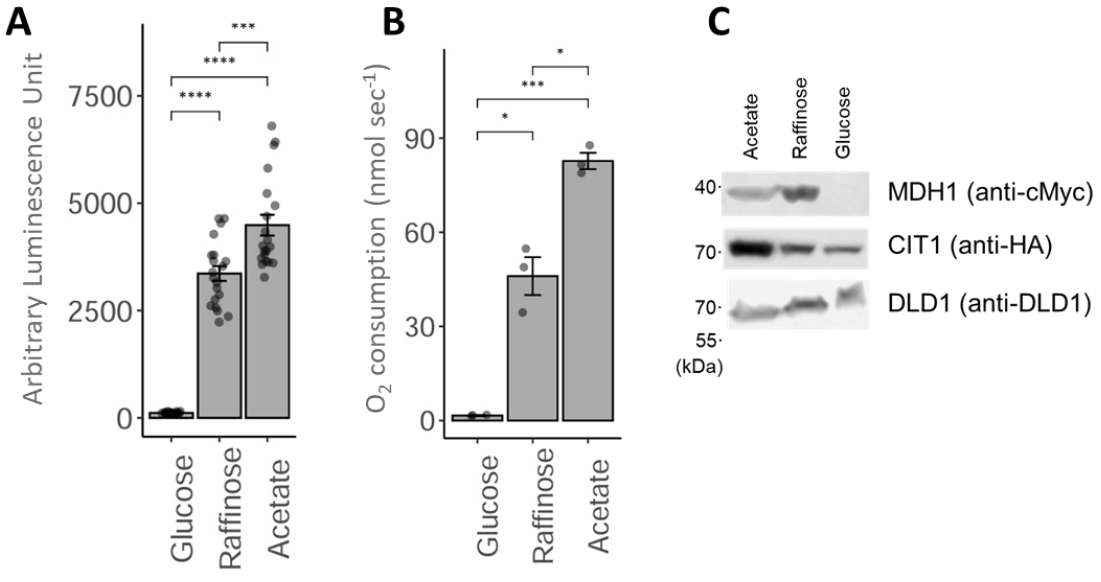

966
967
968 **Figure 1. MDH1-CIT1 interaction under respiration, fermentation, and mixed-respiration**
969 **conditions.** Yeast cells were grown in the minimum media containing acetate (SD-Acet), glucose
970 (SD-Gluc), and raffinose (SD-Raff) to the exponential growth phase. **(A)** Luciferase signal
971 indicating MDH1-CIT1 complex interaction (N=20). **(B)** Cellular oxygen consumption rate (N=3).
972 **(C)** MDH1 and CIT1 protein levels detected by Western blotting. Numbers on the left indicate the
973 position of the molecular weight markers. DLD1 is a loading control of mitochondrial protein. Full
974 gel images are in Figure 1 – figure supplement 2. In A and B, data are presented as mean ±
975 SEM. and the differences between conditions were tested by Student's *t*-test. Asterisks indicate
976 significant differences (*, $p<0.05$; **, $p<0.01$; ***, $p<0.001$; ****, $p<0.0001$; ns, not significant).
977
978 **Figure 1 – figure supplement 1.** Growth rate and enzyme activity of nanoBIT reporter strain.
979
980 **Figure 1 – figure supplement 2.** Full Western blotting image showing MDH1 and CIT1 protein
981 abundance in Figure 1C.
982
983

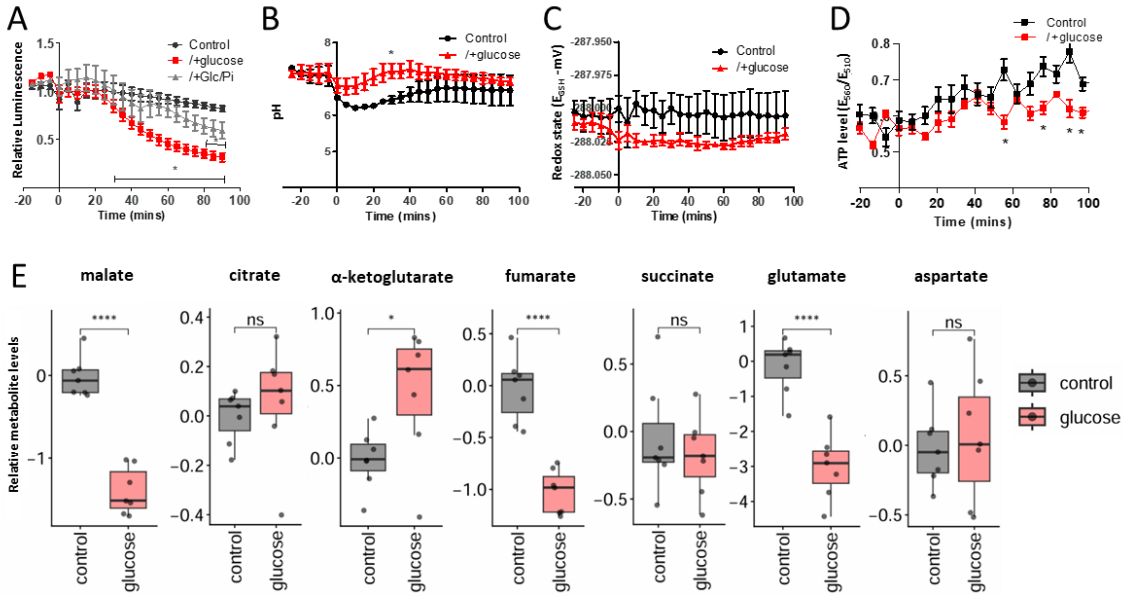

Figure 2. MDH1-CIT1 complex association, mitochondrial microenvironments, and cellular metabolite levels during Crabtree effect induction. Cells were cultured in fresh SD-Raff media in the control condition (black). The Crabtree effect was induced by the 2% glucose application to the SD-Raff-grown cells at 0 min (red). **(A)** NanoBIT signal indicating MDH1-CIT1 interaction. Relative luciferase unit (RLU) was calculated by normalizing the luciferase signals tothe average signals during three pre-treatment time points. SD-Raff-grown cells were also co-treated with 2% glucose and a fermentation inhibitor, 100 mM phosphate, at 0 min (gray). **(B)** Mitochondrial matrix pH. **(C)** Mitochondrial matrix redox states as GSH/GSSG equivalent (mV). **(D)** Mitochondrial matrix ATP level indicated by the ratio between 560 and 510 nm emission signals. All data in A-D are presented as mean ± s.d. (N=4). **(E)** Cellular metabolite levels at 80 min. The boxes, lines, error bars, and points indicate interquartile range, median, minimum, and maximum values, and outliers, respectively (N=7). Statistical differences against the control samples were assessed using the Student's *t*-test at each time point. Asterisks indicate significant differences (*, $p<0.05$; **, $p<0.01$; ***, $p<0.001$; ****, $p<0.0001$; ns, not significant).

Figure 2 – figure supplement 1. MDH1-CIT1 interaction and protein abundance following the application of glucose.

Figure 2 – figure supplement 2. Effects of sugars on MDH1-CIT1 complex assembly and oxygen consumption rate.

Figure 2 – figure supplement 3. Repeated experiments investigating the effects of sugars on MDH1-CIT1 complex assembly and MDH1 and CIT1 protein abundance following the addition of galactose, sucrose, and fructose.

Figure 2 – figure supplement 4. Biosensors indicating mitochondria microenvironments.

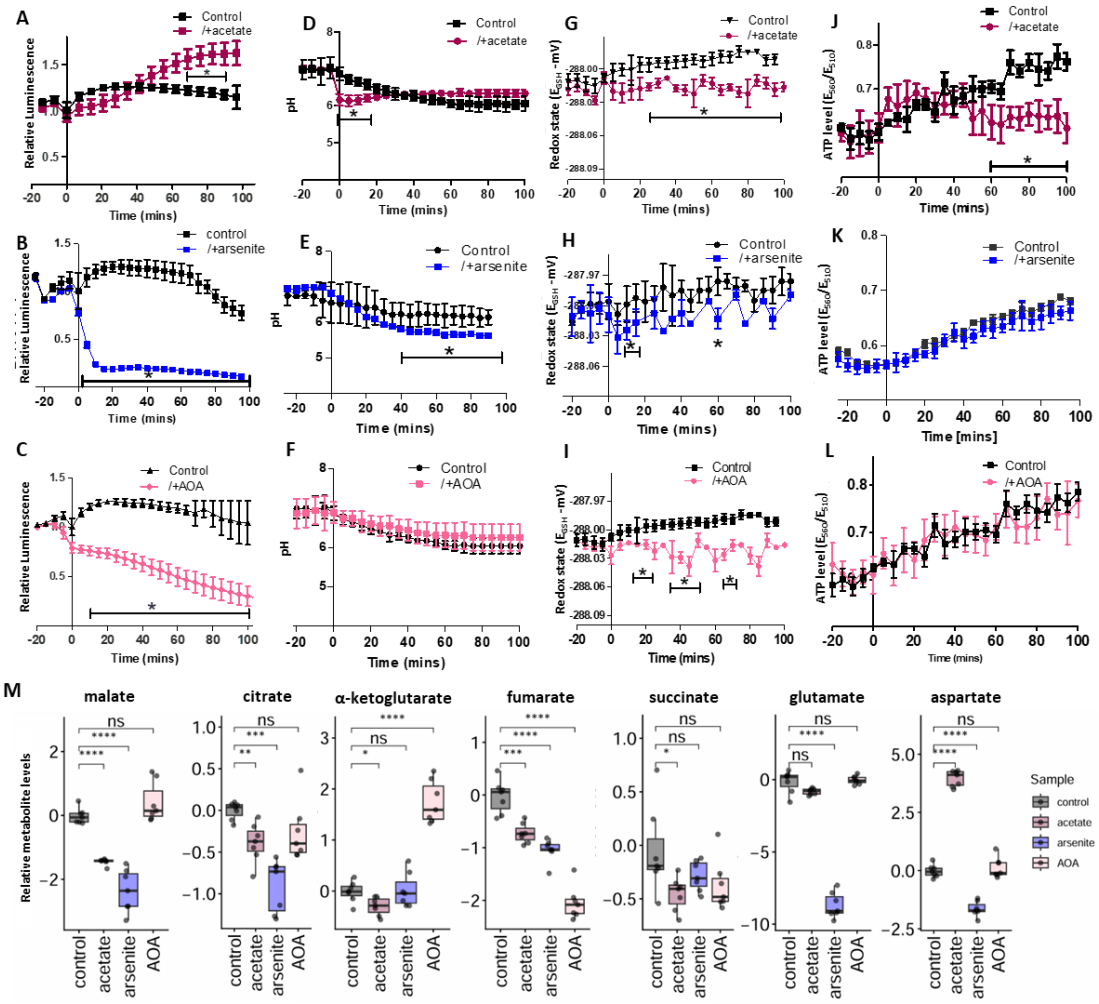

Figure 3. MDH1-CIT1 complex association, mitochondrial matrix microenvironments, and cellular metabolite levels following TCA cycle activation and inhibition. Cells were cultured in SD-Raff media in the control condition (black). The TCA cycle activator (acetate, dark red) and inhibitors (arsenite, blue, and aminooxyacetate (AOA), pink) were applied at 0 min. **(A-C)** NanoBiT signal indicating MDH1-CIT1 interaction. Relative luciferase unit (RLU) was calculated by normalizing the luciferase signals by the average signals during three pre-treatment time points. **(D-F)** Mitochondrial matrix pH in control cells (black) and cells treated with acetate (dark red), arsenite (blue) and AOA (pink). **(G-I)** Mitochondrial matrix redox states as GSH/GSSG equivalent (mV). **(D, H, L)** Mitochondrial matrix ATP level indicated by the ratio between 560 and 510 nm emission signals of mito-GoATeam2 sensor. All data in A-L are presented as mean ± s.d. (N=4). **(M)** Cellular metabolite levels after 80 min of treatment. The boxes, lines, error bars, and points indicate interquartile range, median, minimum, and maximum values, and outliers, respectively (N=7). Statistical differences against the control samples were assessed using the Student's *t*-test at each time point. Asterisks indicate significant differences (*, $p<0.05$; **, $p<0.01$; ***, $p<0.001$; ****, $p<0.0001$; ns, not significant).

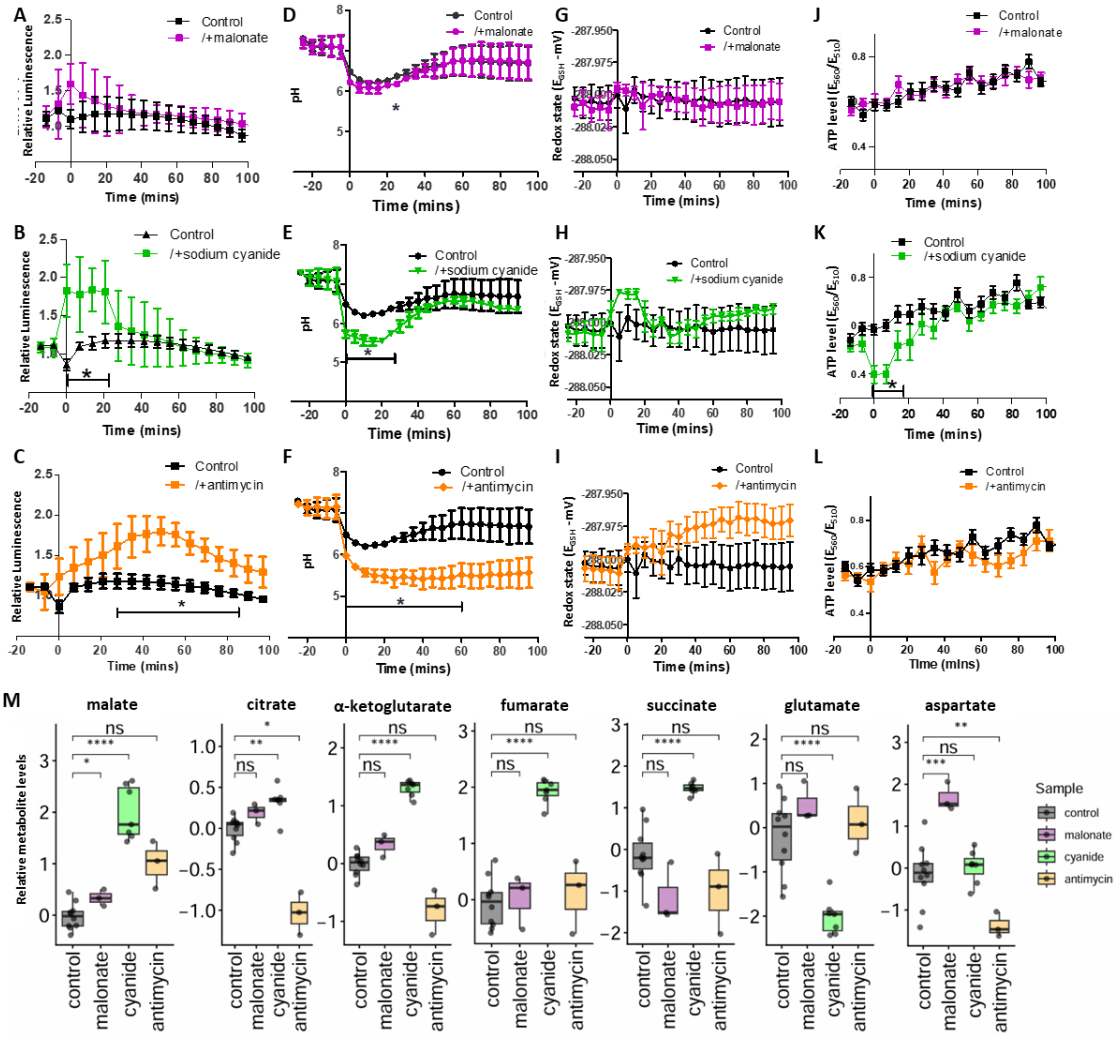

Figure 4. MDH1-CIT1 complex association, mitochondria microenvironments, and cellular metabolite levels following mitochondrial electron transport chain (ETC) inhibition. Cells were cultured in SD-Raff media in the control condition (black). The ETC inhibitors for complex II (malonate, purple, **A-D**), complex IV (cyanide, green, **E-H**), and complex III (antimycin, orange, **I-L**) were applied at 0 min. **(A, E, I)** NanoBiT signal indicating MDH1-CIT1 interaction. Relative luciferase unit (RLU) was calculated by normalizing the luciferase signals by the average signals during three pre-treatment time points. **(B, F, J)** Mitochondrial matrix pH. **(C, G, K)** Mitochondrial matrix redox states as GSH/GSSG equivalent (mV). **(D, H, L)** Mitochondrial matrix ATP level indicated by the ratio between 560 and 510 nm emission signals of mito-GoATeam2 sensor. All data in A-L are presented as mean ± s.d. **(M)** Cellular metabolite levels after 30 min for malonate and cyanide and after 80 min for antimycin treatment. The boxes, lines, error bars, and points indicate interquartile range, median, minimum, and maximum values, and outliers, respectively. Statistical differences against the control samples were assessed using the Student's *t*-test at each time point. Asterisks indicate significant differences with $p<0.05$.

Figure 4 - figure supplement 1. Effect of ETC inhibitors on O_2 consumption rate.

Figure 4 – figure supplement 2. Effects of Complex V inhibition on MDH1-CIT1 complex association, mitochondrial microenvironments, and cellular metabolite levels.

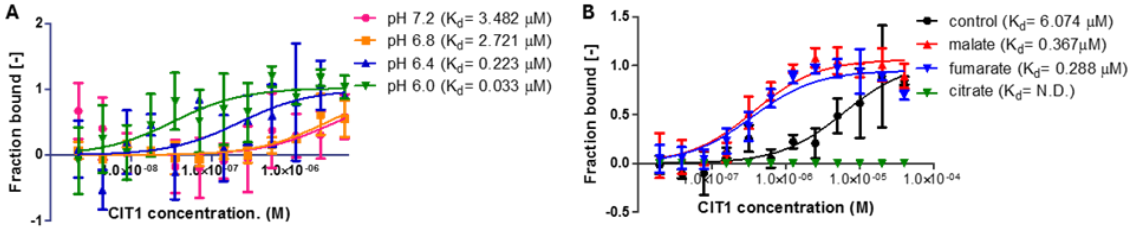

Figure 5. Effects of pH and metabolites on the yeast MDH1-CIT1 multienzyme complex affinity. The affinity of the MDH-CS multienzyme complex was analyzed by microscale thermophoresis (MST) using fluorescently labeled MDH1 as the target and CIT1 as the ligand. Curves represent the response (fraction bound) against CIT1 concentration. Data is presented as mean ± s.d. (N=3). **(A)** Effects of pH. The MDH1-CIT1 interaction was determined in the buffer with pH 7.2 (pink), 6.8 (orange), 6.4 (olive green), 6.0 (green), and 5.8 (blue). **(B)** Effects of 10 mM malate (red), α-ketoglutarate (green), succinate (brown), citrate (blue), aspartate (purple), glutamate (pink), and fumarate (orange). The K_d values of MDH1-CIT1 interaction were shown next to the legend.

Figure 5 – figure supplement 1. Effects of metabolites and ATP on the yeast MDH1-CIT1 multienzyme complex affinity.

A

Treatment	pH	redox	ATP	malate	citrate	αKG	fum	succ	Asp
glucose	↑		↓	↓		↑	↓		
acetate	↓	↓		↓	↓	↓	↓	↓	↑
arsenite	↓	↓		↓	↓	↓	↓		↓
AOA		↓					↓		
malonate	↓			↑					↑
cyanide	↓		↓	↑	↑	↑	↑	↑	
antimycin	↓				↓				↓

B

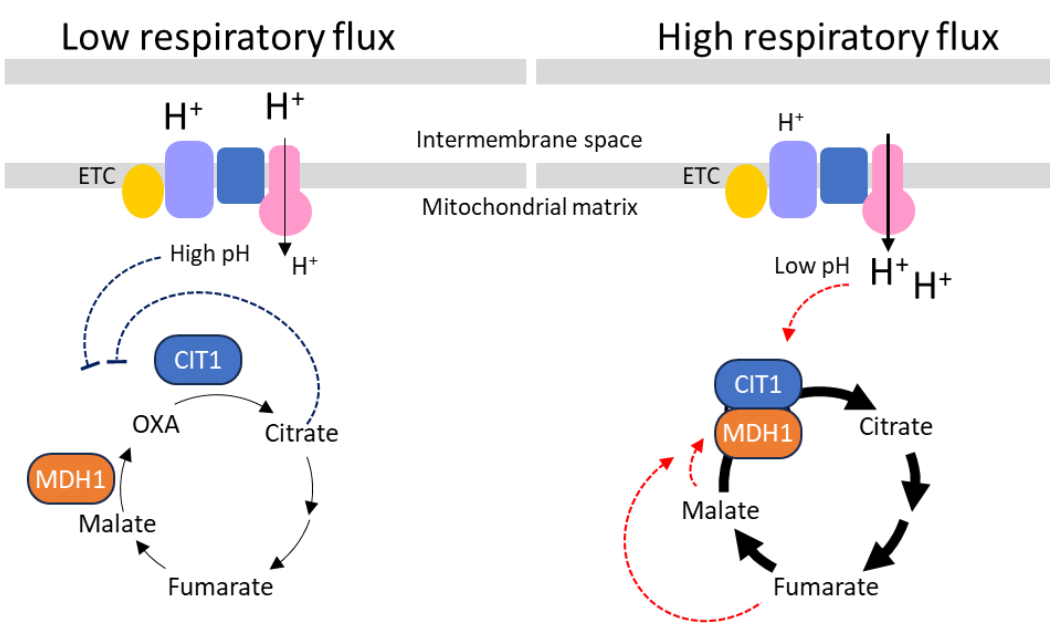

Figure 6. Relationship between the respiratory metabolism and the MDH1-CIT1 metabolon association. (A) Summary of the effects of metabolic treatments on MDH1-CIT1 complex association, mitochondrial matrix parameters (pH, redox state, and ATP levels), and cellular metabolite levels. Each row corresponds to a specific metabolic perturbation. Blue and red labels indicate treatments that decrease or increase the complex association, respectively. Upward and downward arrows indicate increases and decreases in each parameter, respectively. Bold arrows denote changes that are consistent with the observed in vivo alterations in MDH1–CIT1 interaction. The color of the parameter and metabolite indicates its effect on MDH1-CIT1 interaction in vitro (blue, inhibitory; red, promotive). αKG, α-ketoglutarate; fum, fumarate; succ, succinate. **(B)** A diagram depicting the proposed regulatory mechanism of the MDH1-CIT1 metabolon association. In conditions with low respiratory flux, the MDH1-CIT1 multienzyme complex dissociates, and the TCA cycle flux reduces. Reduced ETC flux results in higher mitochondrial matrix pH, which reduces MDH1-CIT1 affinity. When the respiratory flux and the TCA cycle flux are high, MDH1-CIT1 metabolon associates and likely channels the intermediate oxaloacetate (OXA). High ETC flux lowers mitochondrial matrix pH and enhances the MDH1-CIT1 interaction. The TCA cycle intermediates affect MDH1-CIT1 metabolon formation; fumarate and malate enhance (red arrows with dotted lines), and citrate inhibits (blue arrows with dotted lines) the interaction. The arrow thickness represents the metabolic fluxes.

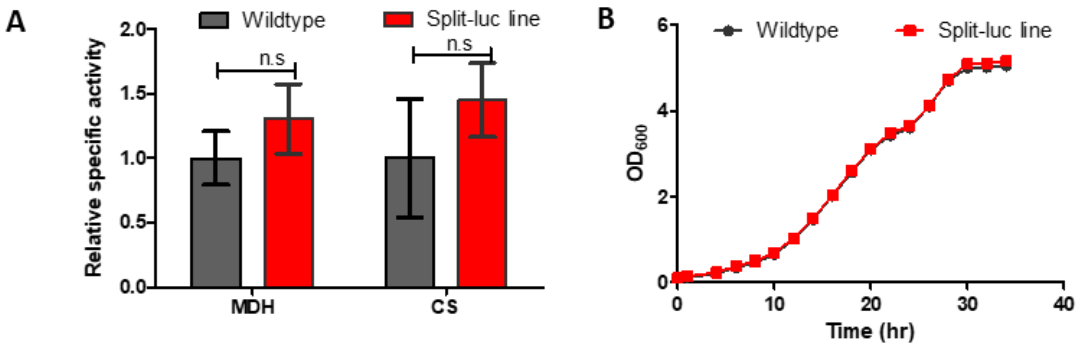

1086

1087 **Figure 1 – figure supplement 1.** Growth rate and enzyme activity of NanoBiT reporter strain. (A)
1088 Extractable cellular MDH and CS enzyme activities in the wildtype (black) and NanoBiT reporter
1089 strain (Split-luc line, red). (B) Growth of cells in SD-raff media monitored as culture OD_{600}. Data
1090 is presented as mean ± s.d. Statistical differences against the wildtype samples were assessed
1091 by Student's *t*-test at each time point. n.s., not significant (p>0.05).

1092

1093

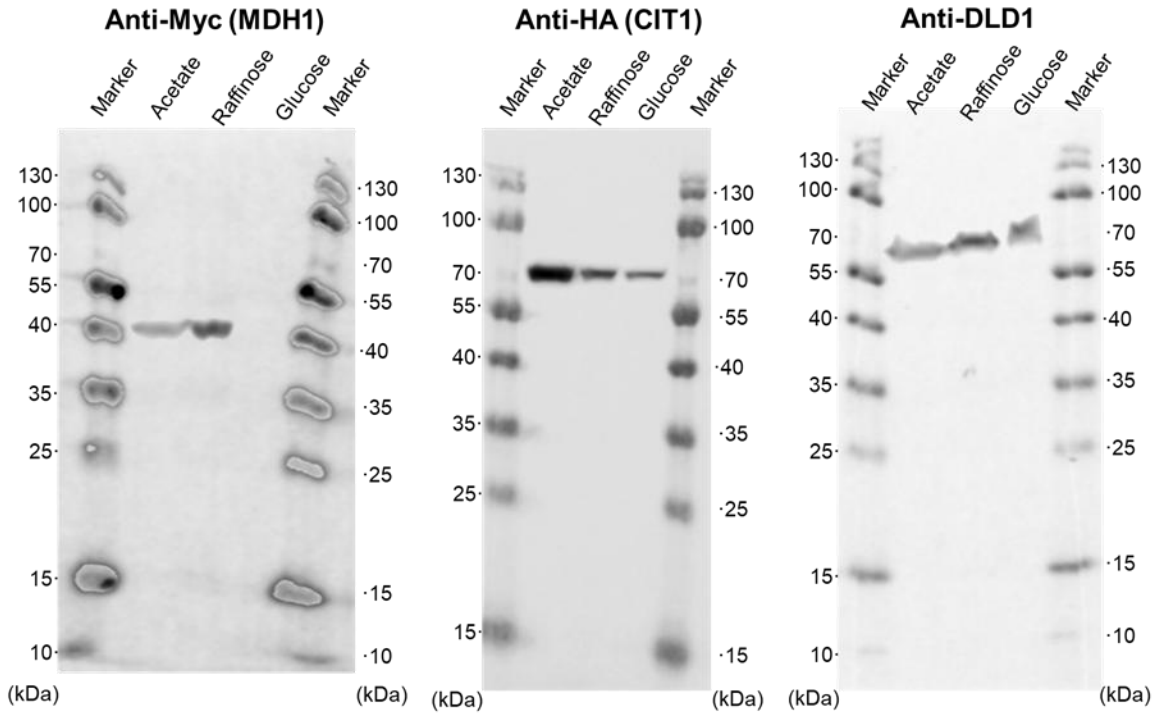

Figure 1 – figure supplement 2. Full Western blotting image showing MDH1 and CIT1 protein abundance in Figure 1C. The numbers on the side of the images indicate the size of the molecular weight markers (kDa).

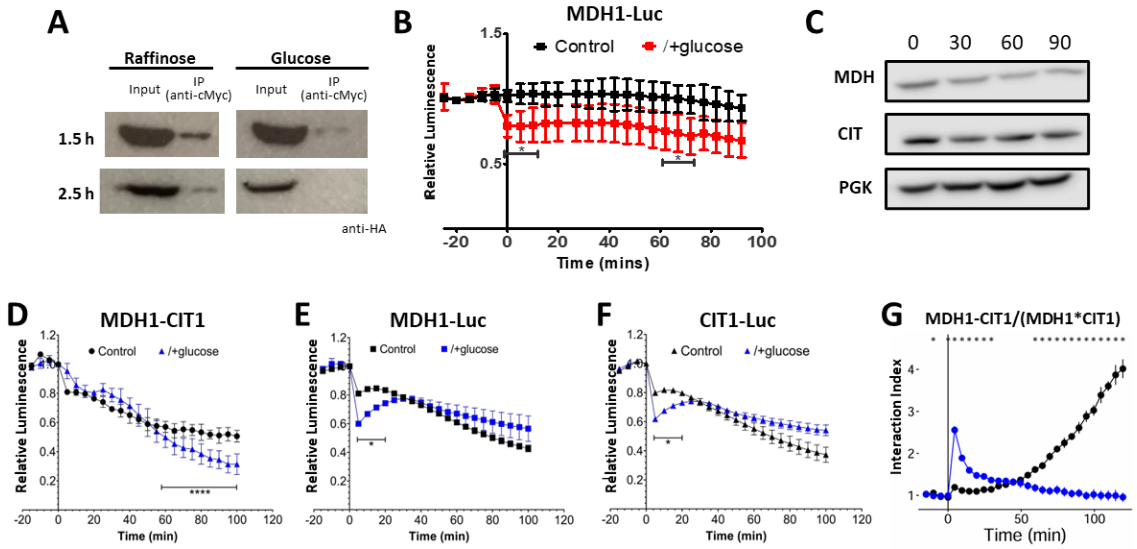

Figure 2 – figure supplement 1. MDH1-CIT1 interaction and protein abundance following the application of glucose. (A) Co-immunoprecipitation of CIT1 with MDH1. In the Split-luc line, MDH1-LgBiT and CIT1-SmBiT harbor cMyc and HA tag in the linker sequence. Proteins were extracted from the Split-luc line grown in SD-faff media at 1.5 and 2.5 hours following 2% glucose application. MDH1 was precipitated with anti-cMyc agarose and co-precipitated CIT1 was detected by anti-HA antibody following SDS-PAGE separation. **(B)** MDH1 protein levels monitored by the luminescence of MDH1 fused with full-length NanoLUC luciferase. **(C)** Western blot analysis of MDH1 and CIT1 protein levels after 0, 30, 60, and 90 min of Crabtree induction. Phosphoglycerate kinase (PGK) was detected as a loading control. **(D)** NanoBIT signal indicating MDH1-CIT1 interaction in a repeated glucose supplementation experiment. SD-Raff-grown cells were treated with 2% glucose at 0 min (blue). **(E)** MDH1 protein levels monitored by the luminescence of MDH1 fused with full-length nanoLUC luciferase in the repeated experiment. **(F)** MDH1 protein levels monitored by the luminescence of CIT1 fused with full-length nanoLUC luciferase in the repeated experiment. Relative luminescence was calculated by normalizing the luciferase signals by the average signals during three pre-treatment time points. Statistical differences against the control samples were assessed by Student's *t*-test at each time point (N=4). Asterisks indicate significant difference (*, $p<0.05$; ****, $p<0.0001$; ns, not significant). **(G)** Interaction index calculated by normalizing NanoBiT signal by those of MDH1-nanoLUC and CIT1-nanoLUC. Asterisks indicate time points with statistically significant differences ($p<0.05$) between control and glucose conditions (N=4).

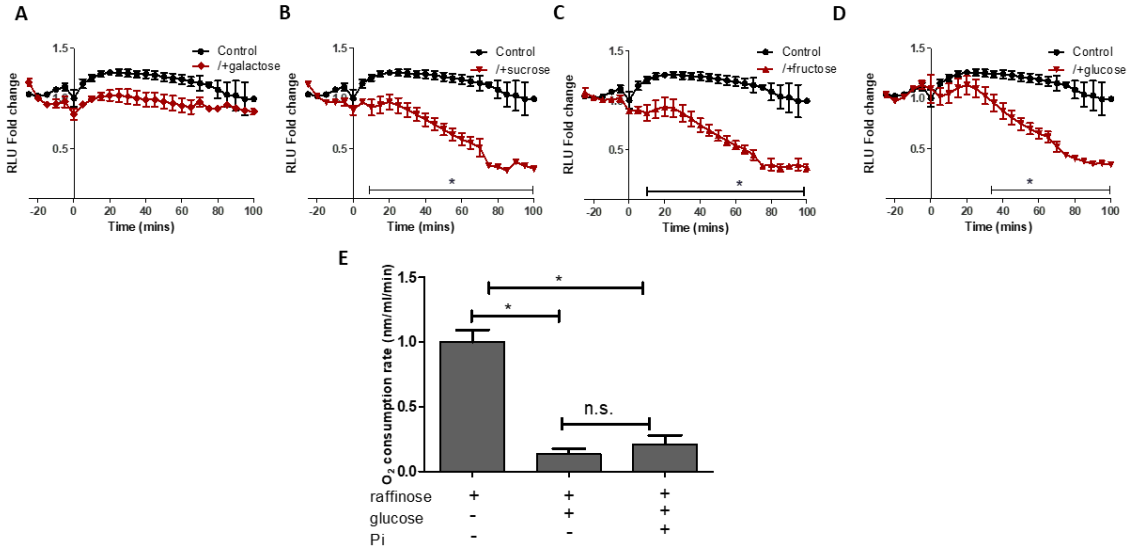

1121

1122 **Figure 2 – figure supplement 2. Effects of sugars on MDH1-CIT1 complex assembly and**
1123 **oxygen consumption rate. (A-D)** NanoBiT signal indicating effect of galactose, sucrose,
1124 fructose, and glucose on MDH1-CIT1 interaction. Cells were cultured in fresh SD-Raff media in
1125 the control condition (black). The cells are treated with 2% sugar application to the SD-Raff-grown
1126 cells at 0 min (red). Relative luciferase unit (RLU) was calculated by normalizing the luciferase
1127 signals by the average signals during three pre-treatment time points. **(E)** Effects of glucose and
1128 inorganic phosphate (fermentation inhibitor) on oxygen consumption rate. Basal O_2 consumption
1129 rate of SD-Raff grown cells was measured. Glucose and inorganic phosphate were added and O_2
1130 consumption rate was measured for 5 minutes. All data in A-E are presented as mean ± s.d.
1131 Statistical differences against the control samples were assessed by Student's *t*-test at each time
1132 point (N=4). Asterisks indicate significant differences with $p<0.05$.

1133

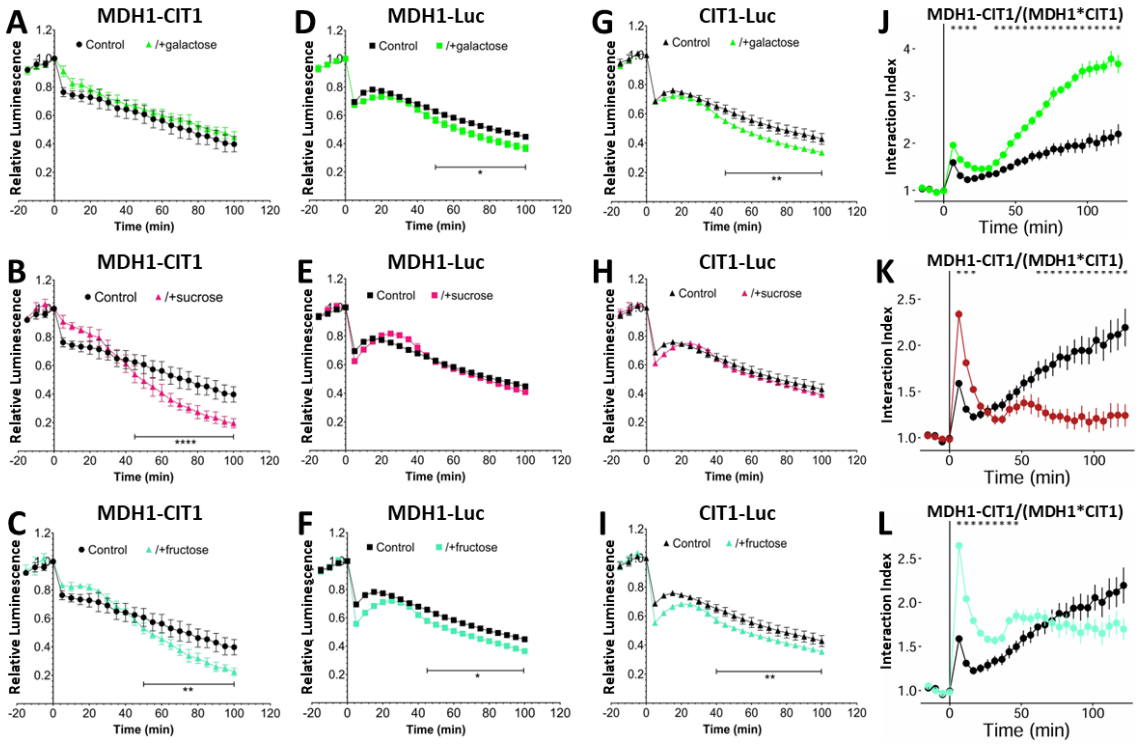

Figure 2 – figure supplement 3. Repeated experiments investigating the effects of sugars on MDH1-CIT1 complex assembly and MDH1 and CIT1 protein abundance following the addition of galactose (green), sucrose (magenta), and fructose (cyan). (A-C) NanoBIT signal indicating effect of galactose **(A)**, sucrose **(B)**, and fructose **(C)** on MDH1-CIT1 interaction. Cells were cultured in fresh SD-Raff media in the control condition (black). The cells are treated with 2% sugar application to the SD-Raff-grown cells at 0 min. Relative luciferase unit (RLU) was calculated by normalizing the luciferase signals by the average signals during three pre-treatment time points. **(D-F)** MDH1 protein levels monitored by the luminescence of MDH1 fused with full-length NanoLUC luciferase. **(G-I)** CIT1 protein levels monitored by the luminescence of CIT1 fused with full-length nanoLUC luciferase. Relative luminescence was calculated by normalizing the luciferase signals by the average signals during three pre-treatment time points. Statistical differences against the control samples were assessed by Student's *t*-test at each time point (N=4). Asterisks indicate significant differences (*, $p<0.05$; **, $p<0.01$; ****, $p<0.0001$). **(J-L)** Interaction index calculated by normalizing NanoBiT signal by those of MDH1-NanoLUC and CIT1-NanoLUC.

1151

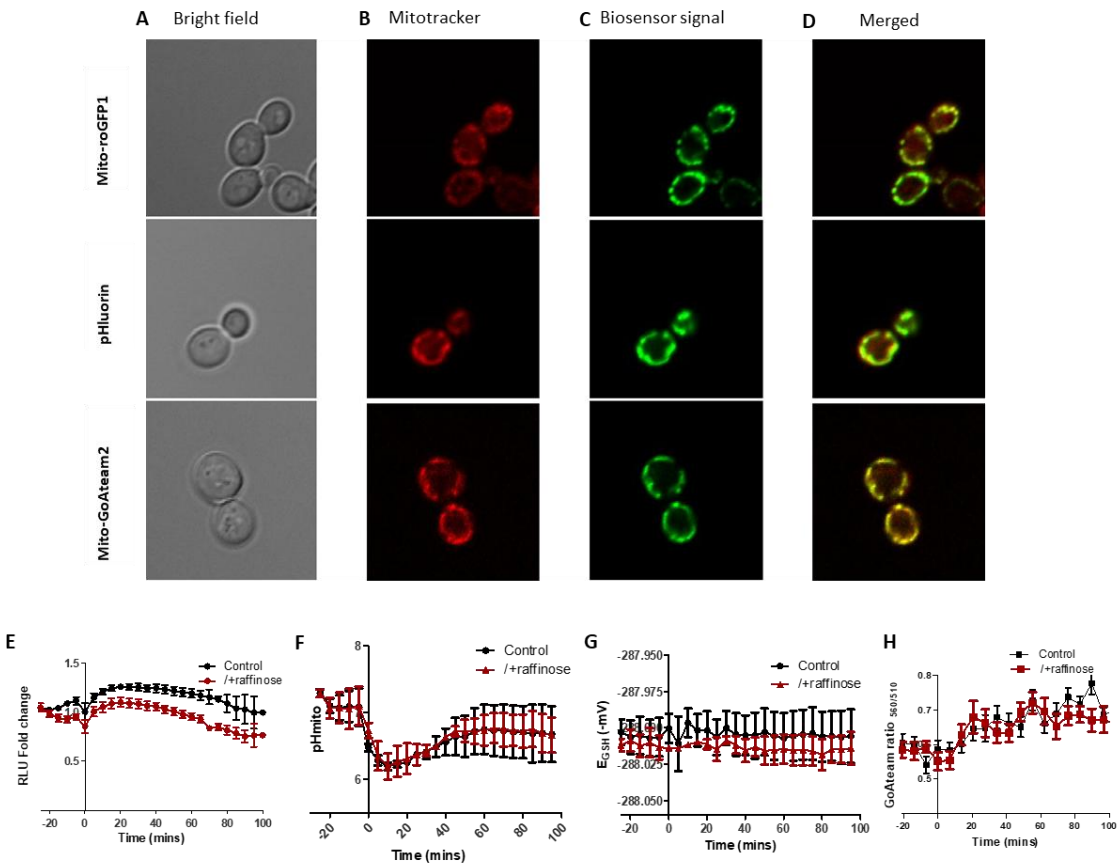

1152

1153 **Figure 2 – figure supplement 4. Biosensors indicate mitochondria microenvironments. (A-**
1154 **D)** Subcellular localizations of fluorescent biosensors. The yeast strains expressing Mito-roGFP1
1155 (upper panels), pHluorin (middle panels), and Mito-GoAteam2 (lower panels) were observed by
1156 fluorescent microscopy in the SD-Raff media. The cells were stained with Mitotracker orange
1157 prior to the analysis. **(A)** Bright field image. **(B)** Mito tracker signal. **(C)** Biosensor signals. **(D)**
1158 Merged images of the A to C. **(E)** Effect of raffinose addition on MDH1-CIT1 interaction. Cells
1159 were cultured in SD-Raff media in the control condition (black). The cells are applied with 2%
1160 raffinose to the SD-Raff-grown cells at 0 min (red). Relative luciferase unit (RLU) was calculated
1161 by normalizing the luciferase signals by the average signals during three pre-treatment time
1162 points. **(F)** Mitochondrial matrix pH in control cells (black) and cells applied with additional
1163 raffinose (red). **(G)** Mitochondrial matrix redox state reported as redox potential of roGFP1 (mV).
1164 **(H)** Mitochondrial matrix ATP level indicated by the ratio between 560 and 510 nm emission
1165 signals of mito-GoATeam2 sensor. Data in E-H are presented as mean ± s.d. (N=4). No
1166 statistical difference was detected between the control and raffinose cells.

1167

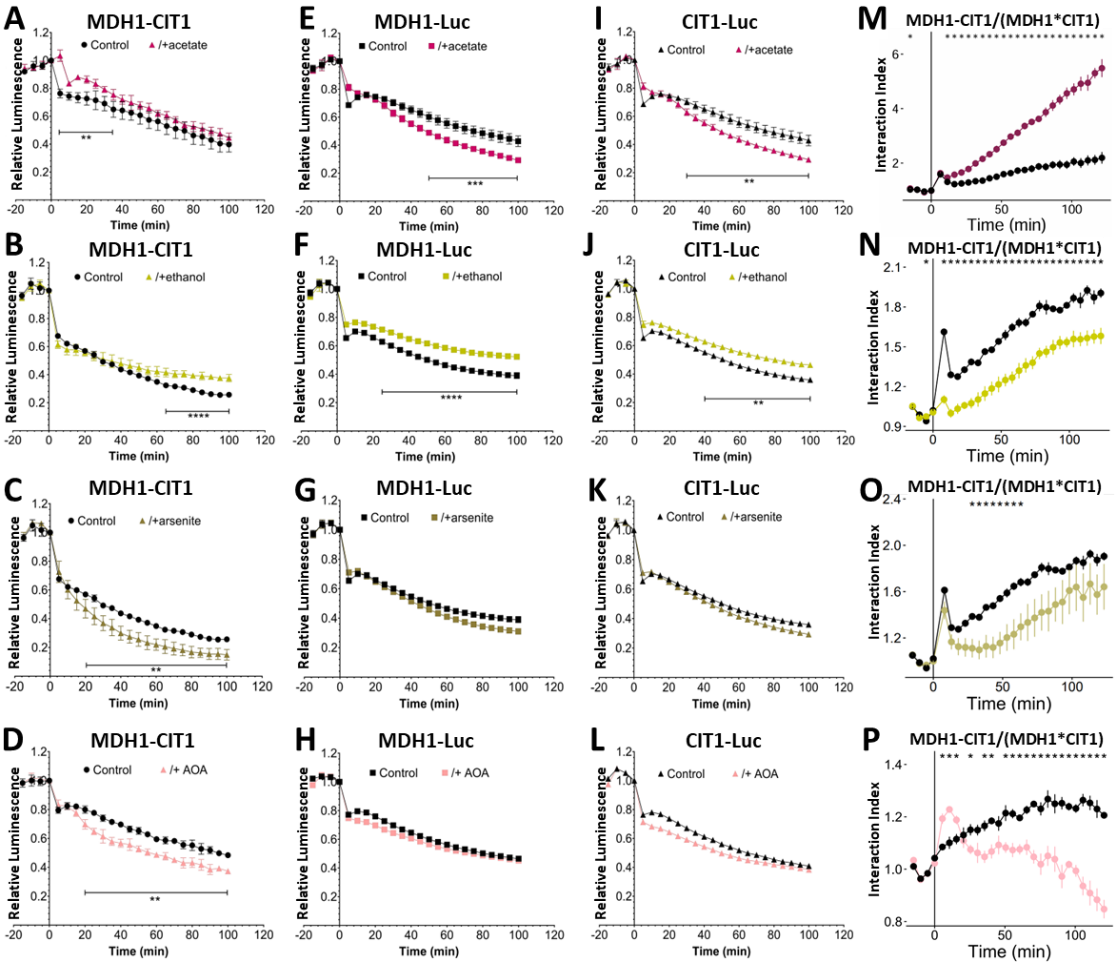

Figure 3 – figure supplement 1. MDH1-CIT1 complex association and MDH1 and CIT1 protein levels following TCA cycle activation and inhibition (repeated experiment). Cells were cultured in SD-Raff media in the control condition (black). The TCA cycle activator (acetate, dark red; ethanol, light yellow) and inhibitors (arsenite, dark yellow; aminooxyacetate, AOA, pink) were applied at 0 min. **(A-D)** NanoBIT signal indicating the MDH1-CIT1 interaction. **(E-H)** MDH1 protein levels monitored by the luminescence of MDH1 fused with full-length NanoLUC luciferase. **(I-L)** CIT1 protein levels monitored by the luminescence of CIT1 fused with full-length NanoLUC luciferase. Relative luminescence Unit (RLU) was calculated by normalizing the luciferase signals by the average signals during three pre-treatment time points. Statistical differences against the control samples were assessed by Student's *t*-test at each time point (N=4). Asterisks indicate significant differences (**, $p<0.01$; ***, $p<0.001$). **(M-P)** Interaction index calculated by normalizing NanoBiT signal by those of MDH1-NanoLUC and CIT1-NanoLUC. Asterisks indicate time points with statistically significant differences ($p<0.05$) between control and treatment conditions (N=4).

1185

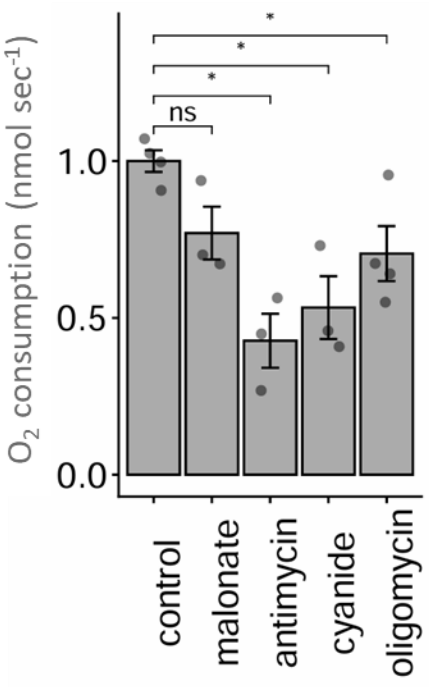

1186

1187 **Figure 4 - figure supplement 1.** Effect of ETC inhibitors on O_2 consumption rate. Basal O_2
1188 consumption rate was measured, then inhibitor was added and O_2 consumption rate was
1189 measured for 5 minutes. Data is presented as mean ± s.d. (N=4), Statistical differences against
1190 the control samples were assessed by Student's *t*-test. Asterisks indicate significant differences
1191 with $p<0.05$.

1192

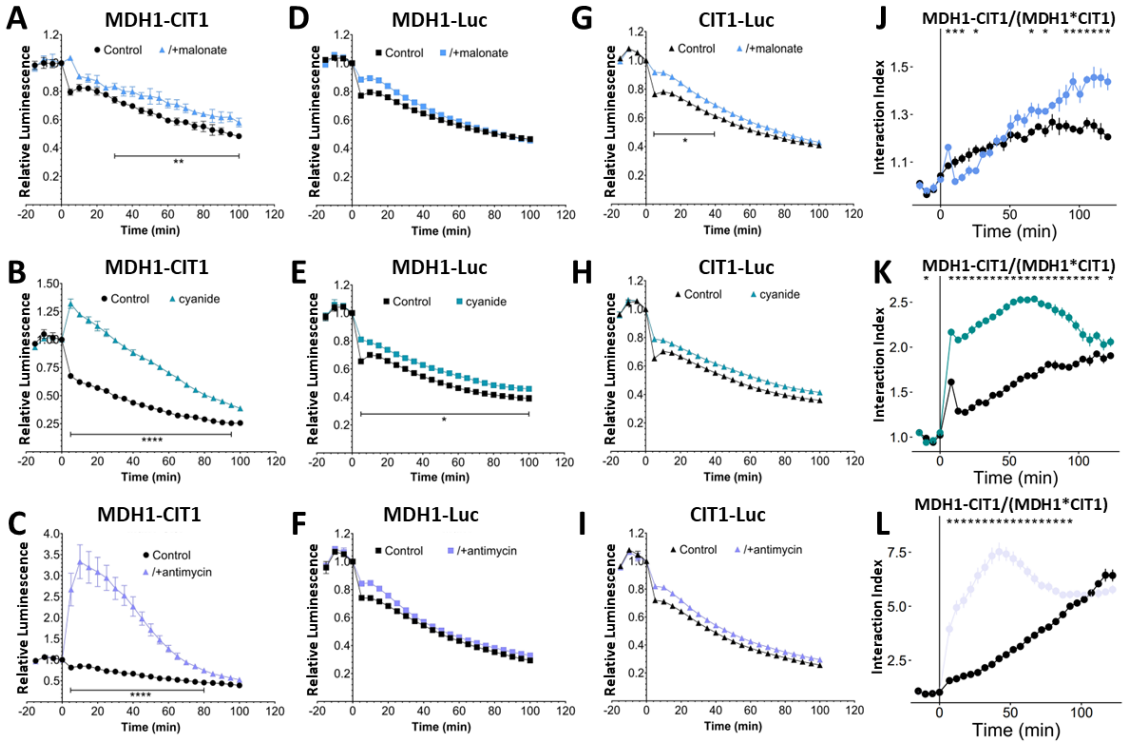

Figure 4 - figure supplement 2. Effect of ETC inhibitors on MDH1-CIT1 complex association and MDH1 and CIT1 protein levels (repeated experiment). Cells were cultured in SD-Raff media in the control condition (black). The electron transport chain inhibitors (malonate, light blue; cyanide, cyan; antimycin, light purple) were applied at 0 min. **(A-C)** NanoBIT signal indicating MDH1-CIT1 interaction. **(D-F)** MDH1 protein levels monitored by the luminescence of MDH1 fused with full-length NanoLUC luciferase. **(G-I)** CIT1 protein levels monitored by the luminescence of CIT1 fused with full-length NanoLUC luciferase. Relative luminescence Unit (RLU) was calculated by normalizing the luciferase signals by the average signals during three pre-treatment time points. Statistical differences against the control samples were assessed by Student's *t*-test at each time point (N=4). Asterisks indicate significant differences (*, $p<0.05$; **, $p<0.01$; ****, $p<0.0001$). **(J-L)** Relative luminescence of the NanoBiT signal normalized by those of MDH1-NanoLUC and CIT1-NanoLUC. Asterisks indicate the time points with statistical significance ($p<0.05$) between control and treatment conditions.

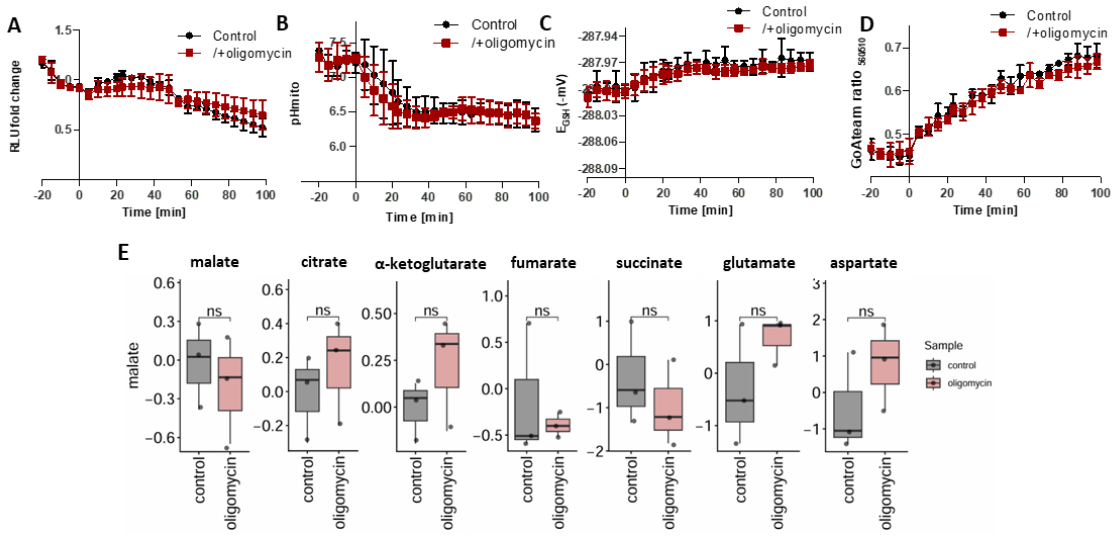

Figure 4 – figure supplement 3. Effects of Complex V inhibition on MDH1-CIT1 complex association, mitochondrial microenvironments, and cellular metabolite levels. Cells were cultured in SD-Raff media in the control condition (black). Oligomycin was applied at 0 min (red). **(A)** NanoBiT signal indicating MDH1-CIT1 interaction. Relative luciferase unit (RLU) was calculated by normalizing the luciferase signals by the average signals during three pre-treatment time points. **(B)** Mitochondrial matrix pH. **(C)** Mitochondrial matrix redox states as GSH/GSSG equivalent (mV). **(D)** Mitochondrial matrix ATP level indicated by the ratio between 560 and 510 nm emission signals of mito-GoATeam2 sensor. All data in A-D are presented as mean ± s.d. (N=4). **(E)** Cellular metabolite levels after 80 min of oligomycin treatment. The boxes, lines, error bars, and points indicate interquartile range, median, minimum, and maximum values, and outliers, respectively. Statistical differences against the control samples were assessed by Student's *t*-test (N=3). No statistical difference was detected between control and oligomycin-treated cells.

1224

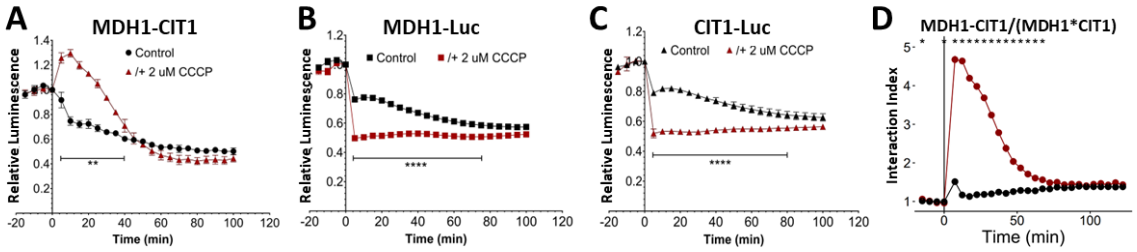

1225 **Figure 4 – figure supplement 4. MDH1-CIT1 complex association and MDH1 and CIT1**
1226 **protein levels following oxidative phosphorylation uncoupler (carbonyl cyanide 3-**
1227 **chlorophenylhydrazone; CCCP) application.** Cells were cultured in SD-Raff media in the
1228 control condition (black). CCCP (dark red) were applied at 0 min. **(A)** NanoBIT signal indicating
1229 MDH1-CIT1 interaction. **(B)** MDH1 protein levels monitored by the luminescence of MDH1 fused
1230 with full-length NanoLUC luciferase. **(C)** CIT1 protein levels monitored by the luminescence of
1231 CIT1 fused with full-length NanoLUC luciferase. Relative luminescence Unit (RLU) was calculated
1232 by normalizing the luciferase signals by the average signals during three pre-treatment time
1233 points. Statistical differences against the control samples were assessed by Student's *t*-test at
1234 each time point (N=4). Asterisks indicate significant differences (**, $p<0.01$; ****, $p<0.0001$). **(D)**
1235 Interaction index calculated by normalizing NanoBiT signal by those of MDH1-NanoLUC and
1236 CIT1-NanoLUC. Asterisks indicate time points with statistically significant differences ($p<0.05$)
1237 between control and CCCP conditions (N=4).

1238

1239

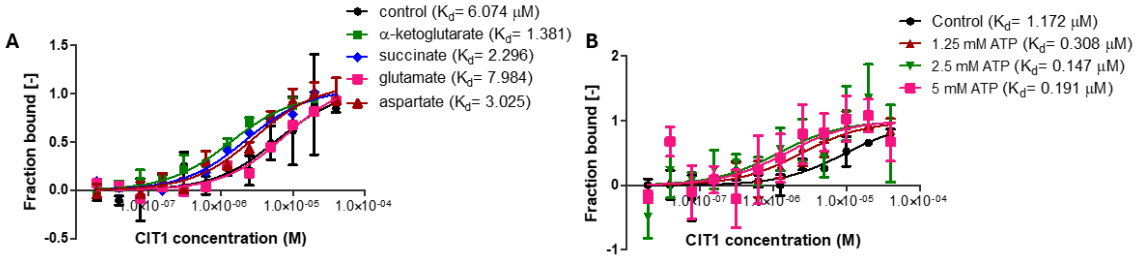

1240 **Figure 5 – figure supplement 1. e**The affinity of the MDH1-CIT1 multienzyme complex was
1241 analyzed by microscale thermophoresis (MST) using fluorescently labeled MDH1 as the target
1242 and CIT1 as the ligand. Curves represent the response (fraction bound) against CIT1
1243 concentration. Points represent the means of fraction bound, and the error bars represent the
1244 standard deviations of three measurements (N=3). **(A)** Effects of metabolites. The MDH1-CIT1
1245 interaction was determined in the buffer (control; black) with 10 mM α-ketoglutarate (green), 10
1246 mM succinate (blue), 10 mM glutamate (pink), and 10 mM aspartate (dark red). **(B)** Effects of
1247 1.25 mM (brown), 2.5 mM (green), and 5 mM (pink) ATP. The K_d values of MDH1-CIT1
1248 interaction were shown next to the legend.

1249

1250 **Supplementary Dataset 1 (separate file). Metabolite profiling data of the *S. cerevisiae* cells.**
1251 The relative metabolite levels were used for the analyses in this study. The raw peak heights,
1252 quantitative ion m/z, and the retention time of the each analyzed peak are also indicated. The
1253 metabolite profiling was conducted in two batchs. CONTROL1, GLUCOSE, CYANIDE,
1254 ACETATE, ARSENITE, and AOA conditions were analyzed in the first batch (N=7). CONTROL2,
1255 MALONATE, OLIGOMYCIN, and ANTIMYCIN were analyzed in the second batch (N=3).
1256